Experimental Neurology 321 (2019) 113040

Contents lists available at ScienceDirect

Experimental Neurology

journal homepage: www.elsevier.com/locate/yexnr

Research paper

# *Sarm1* deletion reduces axon damage, demyelination, and white matter atrophy after experimental traumatic brain injury

Christina M. Marion[a,e], Dennis P. McDaniel[b,c], Regina C. Armstrong[a,d,e,*]

[a] Center for Neuroscience and Regenerative Medicine, F. Edward Hebert School of Medicine, Uniformed Services University of the Health Sciences, Bethesda, MD 20814, USA
[b] Biomedical Instrumentation Center, F. Edward Hebert School of Medicine, Uniformed Services University of the Health Sciences, Bethesda, MD 20814, USA
[c] Department of Microbiology and Immunology, F. Edward Hebert School of Medicine, Uniformed Services University of the Health Sciences, Bethesda, MD 20814, USA
[d] Department of Anatomy, Physiology and Genetics, F. Edward Hebert School of Medicine, Uniformed Services University of the Health Sciences, Bethesda, MD 20814, USA
[e] Program in Neuroscience, F. Edward Hebert School of Medicine, Uniformed Services University of the Health Sciences, Bethesda, MD 20814, USA

ARTICLE INFO

*Keywords:*
SARM1
Sterile alpha and TIR containing motif 1
Axon
Myelin
TBI
White matter
Corpus callosum
Myelin outfoldings
Demyelination
Traumatic axonal injury

ABSTRACT

Traumatic brain injury (TBI) often damages axons in white matter tracts and causes corpus callosum (CC) atrophy in chronic TBI patients. Injured axons encounter irreversible damage if transected, or alternatively may maintain continuity and subsequently either recover or degenerate. Secondary mechanisms can cause further axon damage, myelin pathology, and neuroinflammation. Molecular mechanisms regulating the progression of white matter pathology indicate potential therapeutic targets. SARM1 is essential for execution of the conserved axon death pathway. We examined white matter pathology following mild TBI with CC traumatic axonal injury in mice with *Sarm1* gene deletion (*Sarm1*−/−). High resolution ultrastructural analysis at 3 days post-TBI revealed dramatically reduced axon damage in *Sarm1*−/− mice, as compared to *Sarm1*+/+ wild-type controls. *Sarm1* deletion produced larger axons with thinner myelin, and attenuated TBI induced demyelination, i.e. myelin loss along apparently intact axons. At 6 weeks post-TBI, *Sarm1*−/− mice had less demyelination and thinner myelin than *Sarm1*+/+ mice, but axonal protection was no longer observed. We next used Thy1-YFP crosses to assess *Sarm1* involvement in white matter neurodegeneration and neuroinflammation at 8 weeks post-TBI, when significant CC atrophy indicates chronic pathology. Thy1-YFP expression demonstrated continued CC axon damage yet absence of overt cortical pathology. Importantly, significant CC atrophy in Thy1-YFP/*Sarm1*+/+ mice was associated with reduced neurofilament immunolabeling of axons. Both effects were attenuated in Thy1-YFP/*Sarm1*−/− mice. Surprisingly, Thy1-YFP/*Sarm1*−/− mice had increased CC astrogliosis. This study demonstrates that *Sarm1* inactivation reduces demyelination, and white matter atrophy after TBI, while the post-injury stage impacts when axon protection is effective.

## 1. Introduction

Traumatic brain injury (TBI) is a massive global health issue, with > 27 million new cases annually and an increasing incidence rate (James, 2019). Across the TBI spectrum, long axons within the white matter are especially susceptible to compression, tension, and torsion forces resulting in diffuse axonal injury (Buki and Povlishock, 2006; DiLeonardi et al., 2009; Dileonardi et al., 2012; Johnson et al., 2013b; Smith et al., 2013). Reduced white matter integrity associated with diffuse axonal injury, particularly in the corpus callosum (CC), is often observed in TBI patients and corresponds to worsened outcomes (Adams et al., 1989; Armstrong et al., 2016; Chung et al., 2018; Lipton et al., 2008; O'Phelan et al., 2018; Rutgers et al., 2008). Neuroinflammation and white matter degeneration can persist for years after TBI, and unfortunately CC atrophy is common in patients with chronic symptoms (Hayes et al., 2016; Johnson et al., 2013a; Niogi et al., 2008;

*Abbreviations:* TBI, Traumatic brain injury; CC, Corpus callosum; SARM1, sterile alpha and Toll/interleukin-1 receptor motif-containing 1; NAD+, nicotinamide adenine dinucleotide; NMNAT2, nicotinamide nucleotide adenylyltransferase 2; DLK, dual leucine zipper kinase; LZK, leucine zipper kinase; TIR, Toll interleukin receptor; GFAP, Glial fibrillar acidic protein; Iba1, Ionized calcium binding adaptor molecule 1; TUNEL, Terminal deoxynucleotidyl transferase dUTP nick end labeling; ROI, Region-of-interest; YFP, Yellow fluorescent protein

* Corresponding author at: Department of Anatomy, Physiology and Genetics, Uniformed Services University of the Health Sciences, 4301 Jones Bridge Rd., Bethesda, MD 20814, USA.
*E-mail address:* regina.armstrong@usuhs.edu (R.C. Armstrong).

https://doi.org/10.1016/j.expneurol.2019.113040
Received 14 February 2019; Received in revised form 7 August 2019; Accepted 20 August 2019
Available online 21 August 2019

Tomaiuolo et al., 2012; Willmott et al., 2009).

The progression of white matter injury after TBI is poorly understood. Within white matter tracts, both unmyelinated and myelinated axons are vulnerable to damage by TBI (Mierzwa et al., 2015; Reeves et al., 2012). In addition, TBI induced myelin pathology includes demyelination, which is the loss of myelin around otherwise intact axons, and abnormal myelin structure (Marion et al., 2018; Mierzwa et al., 2015; Sullivan et al., 2013). Myelin enables rapid impulse firing and fast conduction of action potentials, and also provides trophic and metabolic support to axons (Hartline and Colman, 2007; Morrison et al., 2013; Nave, 2010). Therefore, myelin pathology could cause processing speed deficits and expose axons to further damage (Lee et al., 2012; Ontaneda et al., 2017a; Pan and Chan, 2017).

After TBI, axons that are irreversibly damaged undergo Wallerian degeneration, by which the distal process degrades. Wallerian degeneration is executed through a conserved molecular axon death pathway (Coleman and Freeman, 2010; Conforti et al., 2014; Essuman et al., 2017; Gerdts et al., 2016; Pieper and McKnight, 2019). This molecular pathway is of particular interest as a target for acute interventions that could mitigate axon degeneration, including after TBI (Geisler et al., 2019; Henninger et al., 2016; Simon and Watkins, 2018; Ziogas and Koliatsos, 2018). Still, axon preservation alone may not be sufficient to prevent functional deficits after TBI. Myelin pathology, such as demyelination, must also be addressed to enable proper axon function. Additionally, an acute intervention must also mitigate chronic neurodegeneration and reduce atrophy of vulnerable white matter tracts to alter a patient's recovery trajectory and improve clinical outcomes following TBI.

Conserved molecular processes initiate distal axon fragmentation and degeneration when axons fail to have continuous delivery and function of pro-survival factors that maintain nicotinamide adenine dinucleotide (NAD+) levels (Pieper and McKnight, 2019). Nicotinamide mononucleotide adenylyltransferase 2 (NMNAT2), which catalyzes an essential step in NAD+ biosynthesis, is a potent axon pro-survival factor. NMNAT2 localized in vesicles undergoes rapid axonal transport and dual leucine zipper kinase (DLK) and leucine zipper kinase (LZK) promote processes, such as proteosomal degradation, that reduce NMNAT2 levels; soluble NMNAT2 is degraded by Phr1 E3 ligase (Xiong et al., 2012; Babetto et al., 2013; Desbois et al., 2018; Gilley et al., 2019; Neukomm et al., 2017; Summers et al., 2018).

Sterile alpha and Toll/interleukin-1 receptor motif-containing 1 (SARM1) acts down-stream of NMNAT2 to hydrolyze NAD+, which depletes axonal levels and initiates execution of axon degeneration (Essuman et al., 2017; Geisler et al., 2019; Gerdts et al., 2016). Loss of sufficient NAD+ leads to a cascade of ionic imbalance and cytoskeletal/structural destruction within the axon (Gerdts et al., 2015; Gerdts et al., 2016; Gerdts et al., 2013; Summers et al., 2016). *SARM1* has a highly regular and conserved sequence across 107 species, including humans, indicating potential evolutionary pressure to regulate function (Malapati et al., 2017). Specifically, genetic selection has highly purified the *SARM1* Toll interleukin receptor (TIR) domain that uses a conserved glutamic acid to catalytically cleave NAD+ into nicotinamide and ADP-ribose to execute axon degeneration (Essuman et al., 2017; Essuman et al., 2018; Malapati et al., 2017). This enzymatic activity of the SARM1 TIR domain is conserved in bacteria and archaea, indicating a broader cellular role as an enzymatic modulator of NAD+ levels in metabolic and bioenergetic pathways (Essuman et al., 2018). SARM1 differs from other TIR domain containing proteins and so may not serve a similar TIR domain scaffolding function for the innate immune response (Essuman et al., 2018; Malapati et al., 2017). Axon degeneration can also involve external signaling mechanisms, such as death receptor 6 (DR6), which may also act on oligodendrocytes and Schwann cells to modulate myelination (Gamage et al., 2017; Mi et al., 2011).

The current study exploits mice with genetic deletion of *Sarm1* to focus on mechanisms that protect against axon damage, as a critical component of TBI pathophysiology, including analysis of myelin that is required for proper axon function along with white matter atrophy as an indicator of chronic neurodegeneration. In experimental primary axonal injury, such as nerve transection, axon degeneration can be dramatically delayed using genetic approaches to inhibit SARM1 enzymatic activity, with some reports of protection throughout the mouse lifespan (Geisler et al., 2016; Geisler et al., 2019; Gilley et al., 2017; Osterloh et al., 2012). The Wallerian degeneration slow (*WldS*) strain of mice, with a mutation that increases NMNAT activity and slows axon degeneration, exhibit promising results of reduced functional deficits using a blast-mediated TBI model (Yin et al., 2016).

The role of SARM1 is not sufficiently understood in vivo during the complex progression of acute through chronic TBI pathology, which can cause continued damage to vulnerable axons. In the context of acute TBI in mice, *Sarm1* deletion significantly attenuates TBI-induced neurological deficits through 48 h post injury, with transient neurometabolic dysfunction primarily observed at 2 h after injury (Henninger et al., 2016). Furthermore, knocking out *Sarm1* reduces the number of axonal lesions associated with damage between 2 and 48 h after TBI (Henninger et al., 2016; Ziogas and Koliatsos, 2018). However, the majority of axon damage occurs after the initial TBI event and results from secondary mechanisms of damage (Buki and Povlishock, 2006; Marmarou et al., 2005). Studies in an optic nerve stretch model of traumatic axonal injury indicated that axons continue to initiate Wallerian degeneration days and weeks after the initial mechanical insult (Maxwell et al., 2015). Furthermore, later stages can exhibit persistent neuroinflammation and white matter atrophy in TBI patients and in experimental TBI (Johnson et al., 2013a; Marion et al., 2018; Mierzwa et al., 2015). This continued initiation of axonal injury and progression of white matter pathology offers a therapeutic window for intervention that has not been addressed for analysis of *Sarm1*, and warrants further study in TBI more broadly.

The objective of the current study was to test the effects of *Sarm1* genetic deletion relative to TBI induced white matter pathology. At early and late phase post-injury time points, we examined multiple features of axon and myelin pathology. At longer post-injury time points, we sought to test whether *Sarm1* deletion alters neuroinflammation or is sufficient to prevent chronic stage CC atrophy. We used a single impact TBI in mice that produces traumatic axonal injury in the CC, which reflects the susceptibility of long myelinated axons in the human CC after TBI (Marion et al., 2018; Mierzwa et al., 2015; Sullivan et al., 2013; Yu et al., 2017). This TBI model also results in an innate immune response with persistent astrogliosis and microglial activation through at least 6 weeks post-injury (Mierzwa et al., 2015; Sullivan et al., 2013). Significant CC atrophy is not evident at 3 days through 6 weeks yet is observed at 8 weeks post-injury (Mierzwa et al., 2015; Marion et al., 2018). Within the CC, transmission electron microscopy of ultrastructural features identifies a range of TBI induced axon pathology, including disrupted fast axonal transport, compacted cytoskeletal structure, and swollen mitochondria (Mierzwa et al., 2015). Electron microscopy also identifies distinct myelin pathologies that can only be detected and quantified at the ultrastructural level (Marion et al., 2018; Mierzwa et al., 2015). Therefore, the current experiments accurately delineate the effect of *Sarm1* deletion on early and late axonal pathology along with the corresponding myelin pathology after TBI. In addition, this study examines the capacity for *Sarm1* deletion to mitigate chronic stage CC atrophy and the contribution of neuroinflammation in the CC and cerebral cortex. Together these experiments provide a genetic proof-of-concept to evaluate whether blocking activation of the conserved axon death molecular pathway would be beneficial for preserving axonal integrity, preventing demyelination, and/or reducing chronic white matter atrophy after TBI.

## 2. Materials and methods

### 2.1. Mice

All mice were treated in accordance with guidelines of the Uniformed Services University of the Health Sciences and the National Institutes of Health Guide for the Care and Use of Laboratory Animals. Mice were socially housed with 2–5 mice per 35 cm × 16.5 cm × 18 cm cages containing enrichment objects. Mice were maintained on a standard 12 h cycle of daytime light (6:00–18:00) during which all procedures took place. The following mouse strains were obtained from The Jackson Laboratory: *Sarm1* −/− knockout mice B6.129 × 1-*Sarm1*$^{tm1Aidi}$/J (RRID:IMSR_JAX:018069) and Thy1-YFP reporter mice B6.Cg-Tg(Thy1-YFP)16Jrs/J (RRID:IMSR_ JAX:003709). The B6.129 × 1-*Sarm1*$^{tm1Aidi}$/J mice were generated so that *Sarm1* exons 3–6 were replaced with a neomycin resistance gene in reverse orientation and null mice were back-crossed to a C57BL/6 strain (Kim et al., 2007). Pathological evaluation, focused on the brain where *Sarm1* is normally highly expressed, did not identify abnormalities at the gross or microscopic level, and confirmed no SARM1 protein is produced in null mice (Gilley et al., 2015; Kim et al., 2007). To generate experimental mice, *Sarm1* knockout mice were crossed to either C57BL/6J mice or B6.Cg-Tg(Thy1-YFP)16Jrs/J (Thy1-YFP) mice and bred as in-house colonies to generate the experimental littermate mice (*Sarm1* littermates or Thy1-YFP/*Sarm1* littermates). Each mouse had tail snips genotyped at Transnetyx (Cordova, TN) using probes to detect the *Sarm1* wild type allele and for the inserted neomycin cassette in the knockout. The overall number of mice of each genotype was *Sarm1* +/+ (n = 29) and *Sarm1* −/− (n = 27) littermates, and Thy1-YFP/*Sarm1* +/+ (n = 12) and Thy1-YFP/*Sarm1* −/− (n = 9) littermates.

### 2.2. TBI and sham procedures

The TBI procedure followed protocols previously described (Marion et al., 2018; Mierzwa et al., 2015; Yu et al., 2017). This TBI model results in axon pathology in the CC that is most extensive at coronal levels beneath the impact site and is also present in axons in the overlying cingulum (Marion et al., 2018; Sullivan et al., 2013; Yu et al., 2017). Mice received TBI or sham procedures at 8–10 weeks of age. Under isoflurane anesthesia, the scalp was incised along the midline to expose the skull. TBI mice received an impact using a Leica stereotaxic impactor (Leica Biosystems, Buffalo Grove, IL) and 3-mm-diameter tip with velocity set at 4.0 m/s; depth of 1.5 mm; dwell time of 100 ms while sham mice were treated exactly the same but did not receive the TBI impact. Depressed skull fracture and impactor malfunction were predetermined exclusion criterion leading to exclusion of 2 mice. Apnea and righting reflex times were recorded for all mice. Mice were randomly allocated to TBI or sham procedures using the random number generator function in Microsoft Excel. Investigators were blinded to animal injury group allocation and genotype until after data analysis. Mice were analyzed at 3 days (early), 6 weeks (late), and 8 weeks (chronic) after TBI or sham procedures. The 8 week post-injury time point was designated as exhibiting chronic stage white matter injury based on the presence of significant CC atrophy, that was not present in our prior studies at 3 days, 1 week, 2 weeks, or 6 weeks post-injury (Mierzwa et al., 2015; Marion et al., 2018).

The righting reflex was used as a measure of the time the mouse was unresponsive after surgery and serves as an indicator of loss of consciousness. The righting reflex was recorded as the time from the end of anesthesia to the return to the upright position. Righting reflex time did not differ between male and female littermates, so the sexes were combined for analysis by genotype. The righting reflex was significantly slower after TBI as compared to the sham procedure for each genotype in the *Sarm1* +/+ and *Sarm1* −/− littermates (ANOVA One Way; $F(3,52) = 99.65$; $p < .0001$) and for the Thy1-YFP; *Sarm1* crosses (ANOVA One Way; $F(3, 17) = 34.82$; $p < .0001$). The Sidak's adjusted values for each sham/TBI comparison were *Sarm1* +/+ ($p < .001$) and *Sarm1* −/− ($p < .0001$), while the *Sarm1* +/+ and *Sarm1* −/− mice had similar righting reflex delays after TBI ($p = .9980$). The adjusted values for the Thy1 crosses for sham/TBI comparisons were Thy1-YFP/*Sarm1* +/+ ($p < .0001$) and Thy1-YFP/*Sarm1* −/− ($p < .001$) while TBI produced a similar righting reflex delay in both genotypes ($p = .9802$). These data indicate that the concussive TBI caused a significant loss of consciousness. *Sarm1* genotype did not alter this indicator of injury severity, in agreement with a prior study using a different concussive model (Henninger et al., 2016).

### 2.3. Electron microscopy

Transmission electron microscopy was used for high resolution imaging of ultrastructural features of axons and myelin. Mice were anesthetized with ketamine/xylazine before transventricular cardiac perfusion with 4% paraformaldehyde (Electron Microscopy Sciences, Hatfield, PA; Cat #19210) and 2.5% glutaraldehyde (Electron Microscopy Sciences; Cat #16210) in 1 M $PO_4$ at 3 days or at 6 weeks after surgery. The cranium was opened to expose the brain for in situ post-fixation in the fixative solution for 3 h before brains were dissected, hemisected along the midline, and left in fixative overnight. One hemisphere was sectioned (40 μm) as sagittal sections using a Leica vibrating VT-1200 vibratome (Leica Biosystems, Buffalo Grove, IL) and left in fresh fixative overnight before washing with 1 M $PO_4$. Sections were selected for further processing based on localization at the coronal level of the anterior commissure and at parasagittal levels to include the CC over the lateral ventricles. Samples were immersed in 2% osmium tetroxide ($OsO_4$; Electron Microscopy Sciences; Cat #19100) in cacodylate buffer (0.1 M, pH 7.4) for 1 h, then washed again in in cacodylate buffer, dehydrated in ethanol, and infiltrated with Spurr epoxy resin (Electron Microscopy Sciences; Cat #14300). These flat-embedded sagittal sections were then polymerized at 70 °C for 11 h, and thin sections (~70 nm) were cut on an Ultracut UC6 ultramicrotome (Leica Biosystems). Copper grids containing thin sections were post-stained for 20 min in 2% aqueous uranyl acetate (Electron Microscopy Sciences; Cat #22400) and for 5 min in Reynolds lead citrate (Reynolds, 1963). Grids were reviewed on a JEOL JEM-1011 transmission electron microscope (JEOL USA Inc., Peabody, MA). Images from 5000 to 15,000× were captured using an AMT XR50S-A digital camera (Advanced Microscopy Techniques, Woburn, MA).

### 2.4. Immunohistochemistry

Thy1-YFP/*Sarm1* mice were analyzed for pathology at 8 weeks after TBI or sham procedures. Mice were deeply anesthetized and transcardially perfused with 0.1 M PB then 4% paraformaldehyde before brains were excised, dissected, and post-fixed overnight in fixative. After 24 h in 30% sucrose at 4 °C for cryoprotection, brains were embedded in OCT compound (Sakura Finetek, Torrance, CA), and sectioned coronally at 14 μm thickness on a Leica CM 1900 UV cryostat (Leica Biosystems). Axons were immunolabeled with SMI-34 primary mouse monoclonal that detects phosphorylated neurofilament-H (1:500; Biolegend, San Diego, CA; Cat# 835503) followed by incubation with AlexaFluor-555-conjugated secondary antibody (1:400, ThermoFisher Scientific; A-21422, RRID: AB_2535844). Myelin was immunolabeled with a primary mouse monoclonal recognizing myelin oligodendrocyte glycoprotein (MOG) (1:100; Millipore, Burlington, MA; Cat# MAB5680, RRID: AB_1587278) followed by incubation with AlexaFluor-647-conjugated secondary antibody (1: 300, Jackson ImmunoResearch Laboratories, West Grove, PA; Cat# 715-605-151, RRID: AB_2340863). Astrocytes were immunostained with monoclonal mouse antibody against glial fibrillary acidic protein (GFAP) (1:500, Millipore; Cat# MAB3402, RRID: AB_94844) with secondary incubation using AlexaFluor-647-conjugated secondary antibody (1: 300, Jackson ImmunoResearch Laboratories; Cat# 715-605-151, RRID: AB_

2340863). Microglia/macrophages were identified using polyclonal rabbit antibody against ionized calcium binding adaptor molecule 1 (Iba1) (1:1000; Wako, Richmond, VA; Cat# 019-19741, RRID: AB_839504) followed by incubation with AlexaFluor-594-conjugated secondary antibody (1:100, Jackson ImmunoResearch Labs Cat# 711-585-152, RRID: AB_2340621). Sections were counterstained with DAPI (Sigma-Aldrich. St. Louis, MO; D9542) before mounting with Vectashield (Vector Laboratories, Burlingame, CA; Cat# H-1000, RRID: AB_2336789). For terminal deoxynucleotidyl transferase dUTP nick end labeling (TUNEL), we utilized ApopTag Peroxidase In Situ Apoptosis Detection Kit (Millipore; Cat# S7100, RRID: AB_2661855). To assess cytoarchitecture of the cerebral cortex, slides were incubated with NeuroTrace 530/615 red fluorescent Nissl stain (Thermo Fisher Scientific, Waltham, MA; Cat# N21482, RRID: AB_2620170).

### 2.5. Quantification of electron microscopy

In-house bred littermate cohorts consisted of *Sarm1*+/+ sham (n = 10; 4 female, 6 male) and TBI (n = 9; 4 female, 5 male) and *Sarm1*−/− sham (n = 10; 7 female, 3 male) and TBI (n = 10; 5 female, 5 male). Mice were sacrificed at 3 days or at 6 weeks after sham or TBI procedure.

Resin-embedded sagittal 40 μm sections were imaged in bright field on an Olympus IX-70 microscope. Osmium staining of the myelin was used to select the region-of-interest (ROI) to be cut out for thin sectioning and quantitative analysis. The ROI was defined as within the CC in a 0.5 mm rostro-caudal region centered under the coronal level of bregma and approximately 200 μm lateral to bregma. This ROI consistently exhibits dispersed axon damage in this model of TBI based on our prior electron microscopy studies and using CLARITY imaging to visualize the axon damage in Thy1-YFP mice (Marion et al., 2018; Mierzwa et al., 2015). This coronal level under bregma aligns with the impact site on the skull and also corresponds with a relatively well myelinated region of the CC (Reeves et al., 2012; Sturrock, 1980). Adjacent sagittal sections were used to measure the inferior-superior width of CC within the ROI at five points at ~100 μm intervals.

Prepared grids of sagittal sections through the CC were imaged at 5000× magnification. Five or more images per animal were quantified for classification of axon and myelin pathology. Three images per animal were used for morphometry to measure axon diameter and myelin thickness. Within each image a 17 μm × 12.5 μm region was defined as the counting frame, within which > 120 axons were quantified. All axons within the counting frame were classified as intact axons, de/unmyelinated axons, damaged axons, or axons with abnormal mitochondria by an investigator blinded to the TBI/sham condition and genotype. Damaged axons were defined as axons with cytoskeletal changes (microtubule and neurofilament density extremely low or high with irregular spacing) or axons with accumulated vesicles. Axons with mitochondria filling > 50% of the axon cross-section were defined as having abnormal mitochondria. De/unmyelinated axons were manually counted based on a lack of detectable compact myelin and an axon diameter larger than 0.3 μm. Axons without myelin and with a diameter smaller than 0.3 μm were excluded from analysis as potentially unmyelinated fibers that are present in healthy adults (Sturrock, 1980). The designation of de/unmyelinated axon counts is used to include demyelinated axons and large unmyelinated axons, since axons were not followed longitudinally to establish myelination in proximal or distal regions. In conditions with the de/unmyelinated axon values higher in TBI mice compared to the corresponding sham mice, the difference is inferred to be TBI induced demyelination. Myelin thickness was calculated as the average of radial measurements at four points per axon, avoiding areas of tongue processes or fixation artifact (Zhou et al., 2012). Myelin outfoldings were manually counted and identified as myelin sheaths folding back onto one another while extending away from an axon. Myelin outfoldings were measured along the lumen between the two sides of the myelin sheath, and that length was doubled to determine the full length of each myelin outfolding. Additional images were taken at 10,000–15,000× for illustration of pathological features.

### 2.6. Quantification of immunohistochemistry

Cohorts of Thy1-YFP/*Sarm1* littermates underwent either TBI or sham surgery and were perfused for analysis at 8 weeks after the procedure for *Sarm1*+/+ sham (n = 6; 3 female, 3 male) and TBI (n = 6; 1 female, 5 male) along with *Sarm1*−/− sham (n = 4; 1 female, 3 male) and TBI (n = 5; 2 female, 3 male). An additional cohort of *Sarm1* littermates, also aged to 8 weeks after the procedure, were used for neurofilament immunohistochemistry in order to image axons in sagittal sections *Sarm1*+/+ sham (n = 5; 2 females, 3 males) and TBI (n = 5; 2 females, 3 males) along with *Sarm1*−/− sham (n = 3; 1 female, 2 males) and TBI (n = 4; 1 female, 3 males).

Fluorescent images were acquired on an Olympus IX70 microscope using a SPOT RT3 camera (Diagnostic Instruments, Arnold, MD). Intensity values of immunolabeled pixels above background levels were thresholded for quantification using ImageJ (National Center for Microscopy and Imaging Research: ImageJ Mosaic Plug-ins, RRID: SCR_001935). Axons, myelin, astrocyte, and microglial fluorescence thresholding to estimate the immunolabeled area was performed in sagittal sections for axons and in coronal sections for other components, as previously detailed (Armstrong et al., 2006). For TUNEL quantification, tissue sections were digitized on a Zeiss Axio Scan Z.1 (Carl Zeiss) and the number of TUNEL+ cells was counted in the CC and cortex for each section using Zen software (Carl Zeiss, ZEN Digital Imaging for Light Microscopy, RRID: SCR_013672). For sagittal images, the CC ROI was aligned with bregma and extended rostrocaudally ~0.5 mm in sections collected ~200 μm lateral to the midline. For all coronal images quantified, the CC ROI extended from the midline laterally to under the peak of the cingulum at coronal levels between +0.5 and − 0.5 mm relative to bregma. The CC width (superior-inferior thickness) was calculated in these same coronal sections as the average of measurements taken at the midline and bilaterally at ~200 μm lateral to the midline, under the peak of the cingulum, and over the lateral border of the ventricle using MOG staining (Marion et al., 2018; Mierzwa et al., 2015). The cerebral cortex ROI extended from the midline, laterally above the CC and cingulum, and extending from the peak of the cingulum upward to the cortical surface (Yu et al., 2017). Quantification for SMI-34, MOG, Iba1, and GFAP included three or more images collected from at least two tissue sections per mouse. TUNEL+ quantification included at least three full sections.

### 2.7. Statistical analysis

All investigators responsible for data collection and analysis were blinded to the sham or TBI condition and to genotype. Data was analyzed and graphed using GraphPad Prism 8.0 software (RRID: SCR_002798). Sample size for each experiment is detailed above and in each figure legend. Bar graphs show means with standard error of the mean and symbols for individual mouse values. Confidence intervals are provided for the axon diameter values to compare the distribution frequency. One-way ANOVA was used to determine statistically significant differences between the means with correction for multiple comparisons using Sidak's test. A p value < .05 was considered statistically significant.

## 3. Results

### 3.1. Sarm1 genetic deletion dramatically reduces axon damage at 3 days after TBI, but does not prevent mitochondrial swelling

We first asked whether *Sarm1* deletion delays the diverse forms of axon pathology resulting from TBI. We used transmission electron

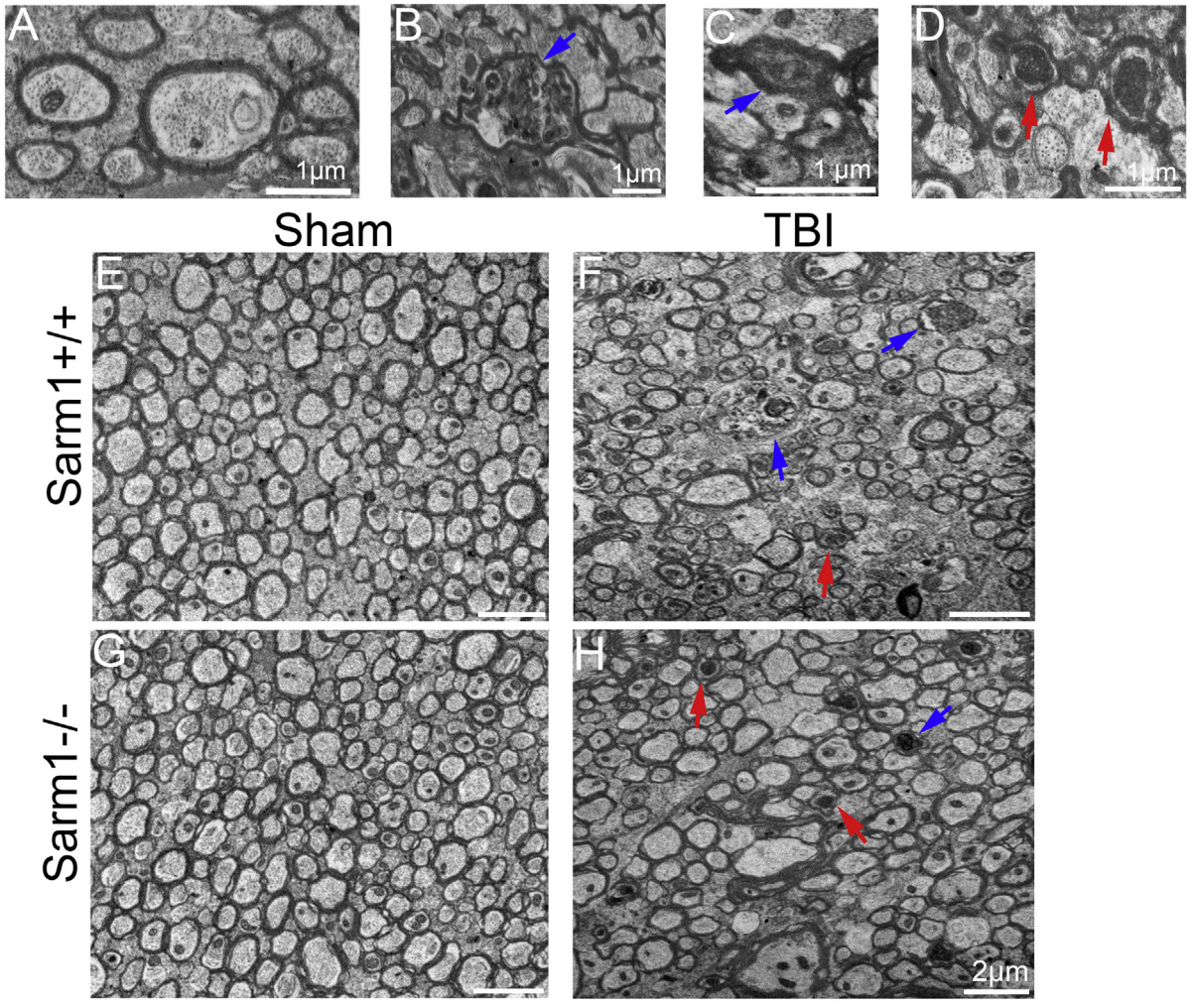


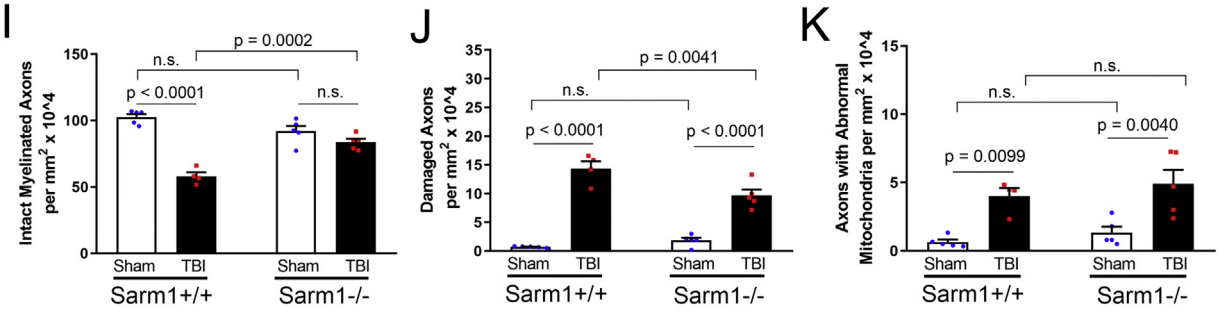


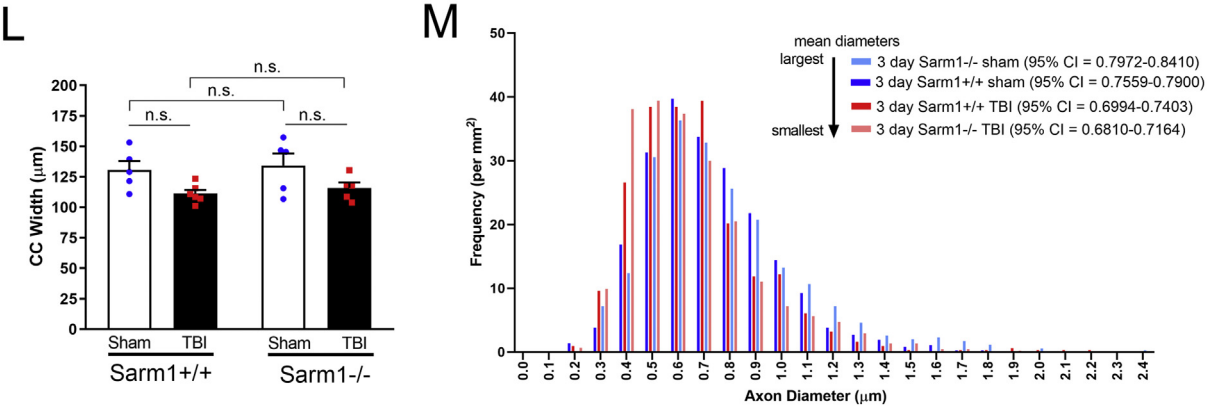


*(caption on next page)*

**Fig. 1.** Axon damage at 3 days after TBI. A–D, High resolution electron microscopy examples of axonal ultrastructure in the corpus callosum (CC) of sham (A) and TBI (B–D) *Sarm1*+/+ mice. A, Intact axons with organized cytoskeletal structure, healthy mitochondrial morphology and compact myelin. B, Damaged axon swollen with accumulated vesicles indicative of disrupted fast axonal transport (blue arrow). C, Damaged axon with collapsed cytoskeleton and condensed cytoplasm (blue arrow). D, Axons with swollen mitochondria (red arrows), which were scored as abnormal if enlarged to > 50% of the axon cross section. E–H, Representative images of sagittal sections through the CC region-of-interest. E, Example of healthy white matter region in *Sarm1*+/+ sham mice showing axons of varied diameter. F, TBI results in dispersed damaged axons (blue arrows) and axons with swollen mitochondria (red arrows) in *Sarm1*+/+ mice. G, *Sarm1*−/− white matter has typical healthy axonal ultrastructure in sham mice. H, *Sarm1*−/− mice exhibit less overall pathology after TBI, although examples of damaged axons (blue arrow) and dispersed axons with swollen mitochondria (red arrows) are still present. I–K, Quantitative analysis of axon pathology in *Sarm1*−/− mice and *Sarm1*+/+ littermates. I, The density of intact axons decreases significantly after TBI in *Sarm1*+/+ mice. More intact axons are preserved after TBI in *Sarm1*−/− mice. J, TBI strongly induces axon damage relative to sham procedures. Axon damage after TBI is significantly reduced in *Sarm1*−/− mice, as compared to *Sarm1*+/+ littermates. K, Axons with abnormal mitochondria are increased after TBI in both *Sarm1*+/+ and *Sarm1*−/− mice. L, TBI does not significantly reduce CC width in mice of either genotype. M, Frequency histogram illustrating the distribution of axon diameters among the myelinated axons counted, which includes intact, damaged, and those with abnormal mitochondria (I–K). The axon populations have a thinner mean diameter after TBI based on non-overlapping 95% confidence intervals (CI). *Sarm1*+/+ n = 5 sham (788 axons), n = 4 TBI (636 axons); *Sarm1*−/− n = 5 sham (736 axons), n = 5 TBI (942 axons). n.s. = not significant. (For interpretation of the references to colour in this figure legend, the reader is referred to the web version of this article.)

microscopy for high resolution analysis of axonal ultrastructure in *Sarm1*−/− null and *Sarm1*+/+ wild type littermate controls after sham or TBI (Fig. 1). A time point of 3 days was selected to capture ongoing TBI-induced Wallerian degeneration in the CC (Marion et al., 2018; Mierzwa et al., 2015; Sullivan et al., 2013). In sham mice, intact axons have organized cytoskeletal structures and healthy mitochondrial morphology (Fig. 1A). After TBI, *Sarm1*+/+ axons show a range of pathological features associated with injury, including swollen axons with accumulated vesicles (Fig. 1B), axons with collapsed cytoskeleton and condensed cytoplasm (Fig. 1C), and axons with swollen mitochondria (Fig. 1D). Sagittal sections through the CC ROI show healthy axons of varied diameter in sham *Sarm1*+/+ mice (Fig. 1E). In contrast, after TBI, dispersed damaged axons and axons with swollen mitochondria are present in *Sarm1*+/+ mice (Fig. 1F). *Sarm1*−/− white matter axons have normal ultrastructure in sham mice (Fig. 1G). After TBI, *Sarm1*−/− mice exhibit less overall axonal pathology (Fig. 1H), which was borne out upon quantitative analysis. TBI significantly reduces the density of intact axons in *Sarm1*+/+ mice, and *Sarm1* deletion improves survival of intact axons (Fig. 1I). TBI induces significant axon damage in mice of both genotypes, however the *Sarm1*−/− mice have significantly less axon damage compared to *Sarm1*+/+ mice (Fig. 1J). Taken together, the increase of intact axons complements the decrease of degenerating axons in *Sarm1*−/− mice, indicating a protective effect of *Sarm1* deletion. Importantly, genetic deletion of *Sarm1* does not alter the density of axons with swollen mitochondria after TBI (Fig. 1K), suggesting mitochondrial abnormalities are upstream or independent from *Sarm1* execution of the axon death pathway. Finally, the width of the CC ROI in these *Sarm1*+/+ and *Sarm1*−/− mice is not significantly different, although slightly reduced after TBI (Fig. 1L), which is in agreement with a shift toward smaller axon diameters after TBI (Fig. 1M).

To demonstrate reproducibility and compare to prior studies that used C57BL/6 mice to assess axonal ultrastructure, we repeated these analyses in C57BL6/J mice along with *Sarm1*−/− mice using cohorts purchased directly from the Jackson Laboratories. We again found that after TBI *Sarm1* deletion significantly attenuates axon damage ($p = .0066$) and does not prevent axons with abnormal mitochondria (Fig. S1A–C).

### 3.2. *Sarm1* genetic deletion reduces demyelination at 3 days post-TBI

Traumatic axonal injury in white matter tracts often involves myelinated axons (Marion et al., 2018; Mierzwa et al., 2015). Therefore, we asked whether the protective effect of *Sarm1* deletion on axons could extend to preservation of myelin, which is critical for maintaining proper axon function. TBI leads to two major myelin pathological features of demyelination and myelin outfoldings (Fig. 2). In the healthy adult mouse CC, the majority of axons larger than 0.3 μm in diameter are myelinated (Sturrock, 1980). TBI can cause demyelination, or loss of myelin, along apparently intact axons that are large enough to be myelinated (Fig. 2A) (Marion et al., 2018; Mierzwa et al., 2015). In the current analysis, we use the term "de/unmyelinated" for axons larger than 0.3 μm and lacking myelin. Myelin outfoldings are long extensions of myelin membrane that fold outward from either intact or damaged axons (Fig. 2B) (Mierzwa et al., 2015; Sullivan et al., 2013). We assessed these myelin pathological features at 3 days after sham or TBI procedures, when each has previously been found to be prevalent (Mierzwa et al., 2015). Sham *Sarm1*+/+ mice have a high density of myelinated axons in the CC ROI (Fig. 2C). Comparatively, TBI in *Sarm1*+/+ mice causes demyelination of apparently intact axons as well as myelin outfoldings (Fig. 2D). The *Sarm1*−/− sham mice do not exhibit overt changes in the pattern of myelination (Fig. 2E). In the *Sarm1*−/− mice, less overall TBI related white matter pathology is apparent, although demyelinated axons and myelin outfoldings are present (Fig. 2F).

Quantitative analysis was performed to determine the TBI induced myelin pathology relative to sham mice for each genotype. TBI induced demyelination can be inferred when the de/unmyelinated axons are increased relative to the sham mice. TBI significantly increases demyelinated axons in *Sarm1*+/+, based on de/unmyelinated axons being increased 156.3% over the sham level (Fig. 2G). In contrast, in *Sarm1*−/− mice de/unmyelinated axons increased only 23.0% over shams (Fig. 2G). This data demonstrates that *Sarm1* deletion not only attenuates axon damage but also prevents TBI induced myelin loss along intact axons. TBI increases myelin outfoldings to a similar extent in both *Sarm1*+/+ and *Sarm1*−/− mice, as compared to each sham condition (Fig. 2H). However, the myelin outfoldings are distinctively shorter in *Sarm1*−/− mice than in *Sarm1*+/+ mice (Fig. 2I). Myelin outfoldings extended several microns in length and did not appear to be simply collapsed myelin sheaths of degenerating axons (Fig. 2J).

Consistent with these results, analysis of myelin pathology in an independent cohort also demonstrated that TBI increases demyelinated axons in C57BL/6 J mice, since de/unmyelinated axons increased 145.4% over shams, but not in *Sarm1*−/− mice that increased only 14.3% over shams (Fig. S1D). Also in agreement with the above results, TBI induces myelin outfoldings to similar levels in both genotypes (Fig. S1E). These findings indicate that demyelination and myelin outfoldings may involve distinct processes relative to the progression of axon damage after TBI.

The relationship between *Sarm1* deletion and myelination was further examined by measuring myelin thickness, which is typically proportional to axon diameter in healthy adults. The *Sarm1*−/− mice have thinner myelin relative to axon diameter when compared to the *Sarm1*+/+ mice in both the sham condition and after TBI (Fig. 2K). Using the g-ratio as another method to evaluate myelination status, thinner myelin is found in *Sarm1*−/− mice compared to *Sarm1*+/+ mice in the sham condition but not after TBI (Fig. S2A). At this 3 day post-injury time point, TBI does not significantly change myelin thickness relative to axon diameter when compared to sham mice, regardless of genotype (Fig. 2K). Lack of an effect of TBI on myelin

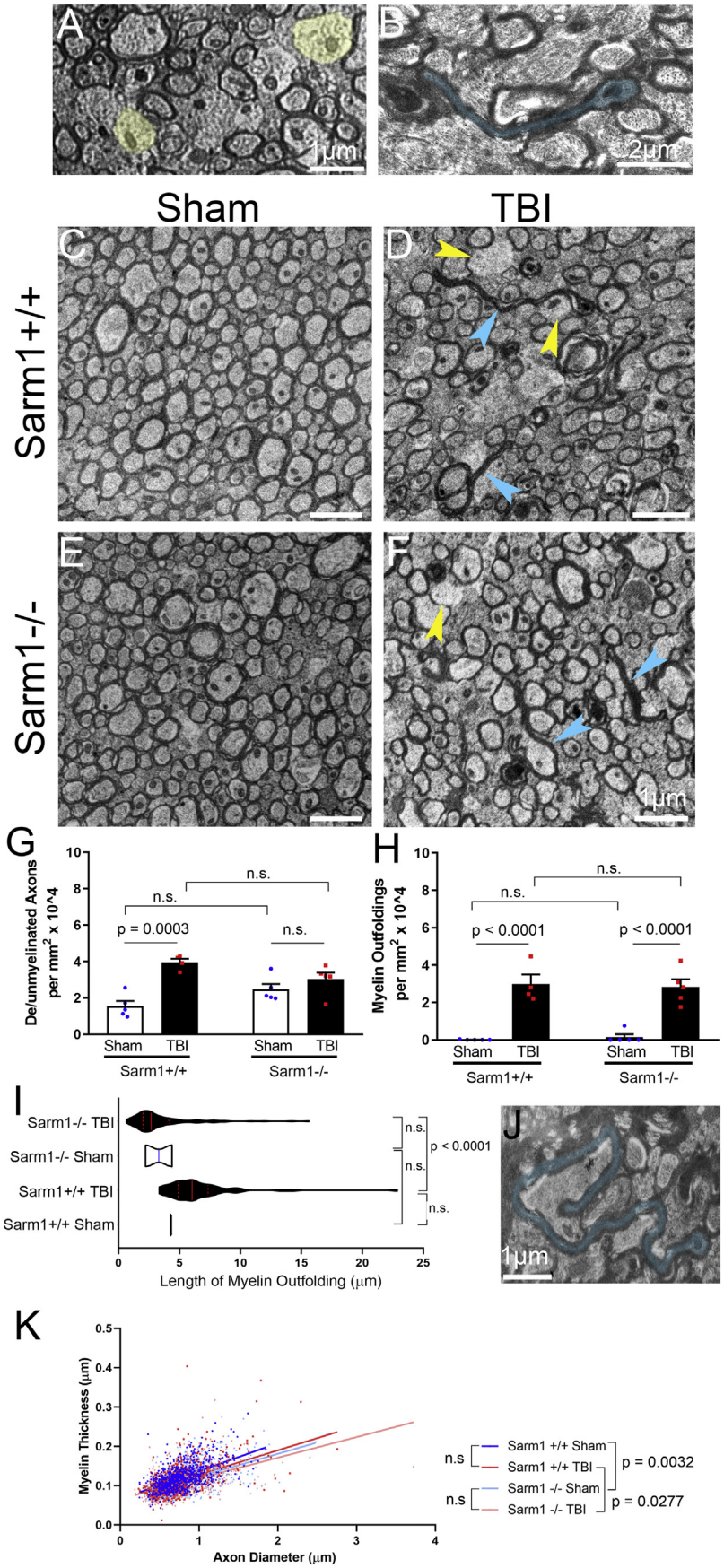


**Fig. 2.** Myelin pathology at 3 days after TBI. A–B, Transmission electron microscopy images from the corpus callosum (CC) showing examples of two major forms of myelin pathology observed at 3 days after TBI in *Sarm1*+/+ mice. A, Demyelinated axons (yellow fill) with intact axonal ultrastructure yet lacking myelin sheaths. B, Myelin outfolding (blue fill) comprised of compact myelin extending away from an axon, which is a condensed degenerating axon in this example. C–F, Representative images of sagittal sections through the CC region-of-interest. C, Example of healthy white matter region in *Sarm1*+/+ sham mice showing high density of myelinated axons. D, TBI causes demyelination of apparently intact axons (yellow arrowheads) and myelin outfoldings (blue arrowheads) in *Sarm1*+/+ mice. E, *Sarm1*−/− white matter has a myelination pattern similar to *Sarm1*+/+ littermates for the sham condition. F, *Sarm1*−/− mice exhibit less overall white matter pathology, although relatively sparse demyelinated axons (yellow arrowhead) and myelin outfoldings (blue arrowheads) are still readily observed. G–I, Quantitative analysis of myelin pathology in *Sarm1*−/− and *Sarm1*+/+ littermates. G, The density of de/unmyelinated axons is significantly increased in TBI versus sham in *Sarm1*+/+ mice, but not in *Sarm1*−/−. This increase is inferred to reflect TBI induced demyelination in the *Sarm1*+/+ mice. H, *Sarm1*+/+ and *Sarm1*−/− mice exhibit myelin outfoldings after TBI. I, The length of myelin outfoldings is reduced in *Sarm1*−/− mice, as compared to *Sarm1*+/+. J, Example of one of the longest myelin outfoldings (blue shading) from a *Sarm1*+/+ mouse. K, Myelin thickness increases with axon diameter. *Sarm1*−/− mice have significantly reduced slopes compared to *Sarm1*+/+ mice in both sham and TBI conditions, indicating thinner myelin relative to axon diameter. *Sarm1*+/+ n = 5 sham (788 axons), n = 4 TBI (636 axons); *Sarm1*−/− n = 5 sham (736 axons), n = 5 TBI (942 axons). n.s. = not significant. (For interpretation of the references to colour in this figure legend, the reader is referred to the web version of this article.)

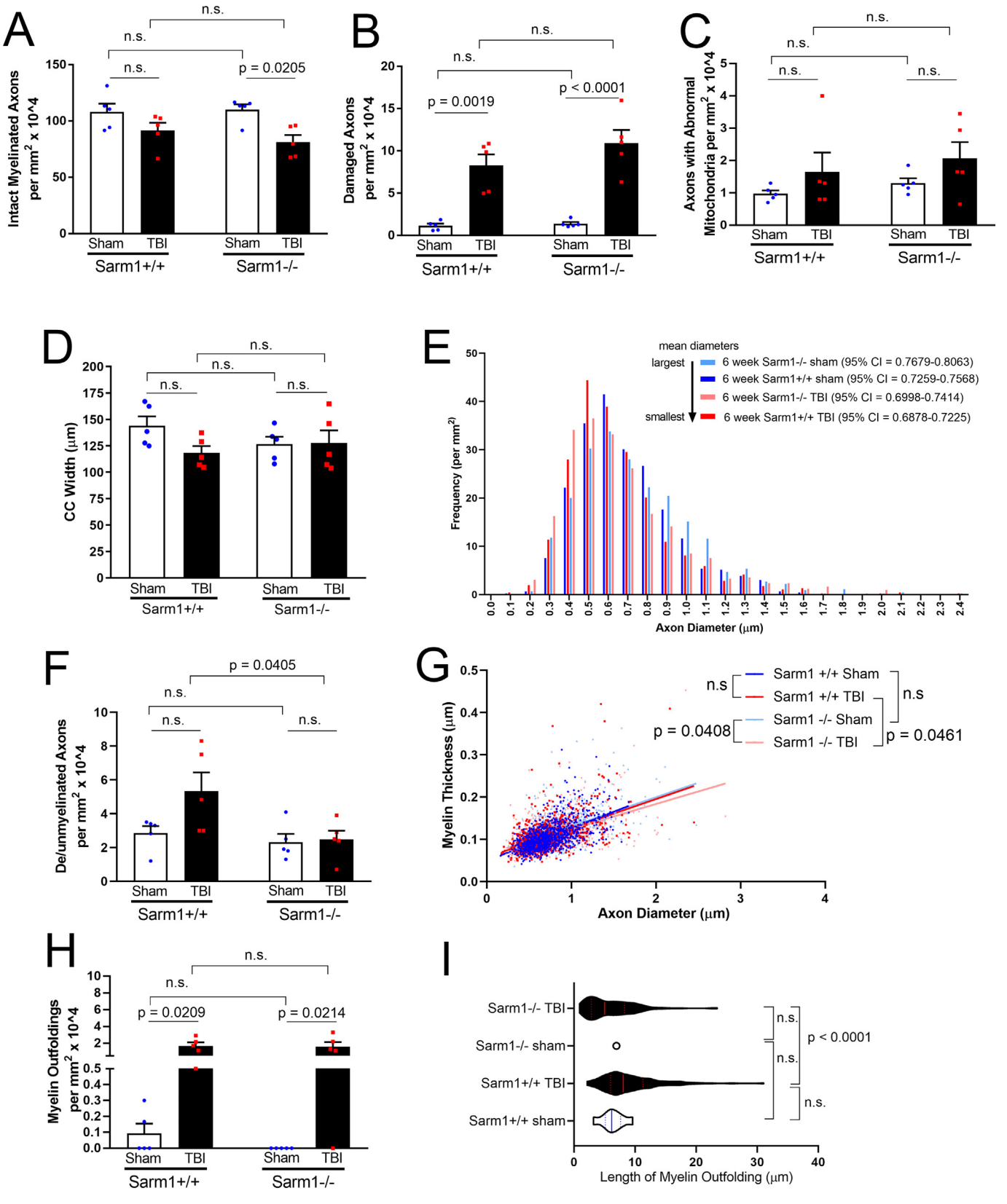


*(caption on next page)*

**Fig. 3.** Axon and myelin pathology at 6 weeks after TBI in *Sarm1* −/− mice and *Sarm1* +/+ littermates. A, The density of intact axons decreases significantly after TBI in *Sarm1* −/− mice. B, TBI strongly induces axon damage relative to sham procedures. C, Axons with abnormal mitochondria are not significantly different after TBI. D, TBI does not significantly reduce corpus callosum (CC) width in mice of either genotype. E, Frequency histogram illustrating the distribution of axon diameters among the myelinated axons counted, which includes intact, damaged, and those with abnormal mitochondria (A–C). E, Axon populations have a smaller mean diameter after TBI based on non-overlapping 95% confidence intervals (CI) relative to sham mice of each respective genotype. F, The density of de/unmyelinated axons after TBI in *Sarm1* +/+ mice is significantly reduced in *Sarm1* −/− mice. G, The TBI *Sarm1* −/− mice have thinner myelin in comparison with sham *Sarm1* −/− and with TBI *Sarm1* +/+ mice. H, *Sarm1* +/+ and *Sarm1* −/− mice exhibit myelin outfoldings after TBI. I, The length of myelin outfoldings after TBI is reduced in *Sarm1* −/− mice, as compared to *Sarm1* +/+. *Sarm1* +/+ n = 5 sham (987 axons), n = 5 TBI (971 axons); *Sarm1* −/− n = 5 sham (953 axons), n = 5 TBI (901 axons). n.s. = not significant. (For interpretation of the references to colour in this figure legend, the reader is referred to the web version of this article.)

thickness at 3 days post-injury is in agreement with our prior results in C57BL/6 mice (Mierzwa et al., 2015).

### 3.3. Sarm1 genetic deletion reduces demyelinated but not damaged axons at 6 weeks post-TBI

We next examined the effects of *Sarm1* deletion on axon and myelin parameters during the progression of white matter injury at a later stage after TBI (Fig. 3). The time point of 6 weeks post-injury was selected to capture continued axon damage and myelin pathology, and also provide time for potential myelin remodeling or repair, i.e. remyelination, based on our prior studies (Marion et al., 2018; Mierzwa et al., 2015). Intact axon densities are very similar in *Sarm1* +/+ and *Sarm1* −/− mice in the sham condition (Fig. 3A). However, a significant population of damaged axons is present in both *Sarm1* +/+ and *Sarm1* −/− mice after TBI, indicating a lack of axon protection from *Sarm1* deletion (Fig. 3B). Axons with abnormal mitochondria, an early feature of axon damage, are not increased after TBI at this 6 week time point (Fig. 3C). The CC width is not significantly changed by TBI at this late post-injury stage (Fig. 3D). However, TBI mice have reduced diameters among the axon populations compared to sham mice of each respective genotype (Fig. 3E).

TBI induced demyelination is significantly less frequent in the *Sarm1* −/− mice than in the *Sarm1* +/+ mice (Fig. 3F). Furthermore, TBI in the *Sarm1* −/− mice results in thinner myelin in comparison to either the corresponding sham mice (Fig. 3G) or *Sarm1* +/+ mice with TBI (Fig. 3G). This thinner myelin is proportional to changes in axon diameter since the g-ratio measure did not reveal significant differences of the *Sarm1* −/− mice after TBI as compared to the other conditions in this 6 week data (Fig. S2). In agreement with our findings at 3 days post-TBI (Fig. 2I, J), myelin outfoldings were significantly increased at 6 weeks after TBI in mice of both genotypes (Fig. 3H) and the lengths were shorter in *Sarm1* −/− mice (Fig. 3I).

### 3.4. Sarm1 genetic deletion reduces corpus callosum atrophy in chronic TBI

Our prior studies found that significant CC atrophy was not observed through 6 weeks post-TBI but was present at 8 weeks (Marion et al., 2018; Mierzwa et al., 2015). Therefore, we examined this 8 week time point as reflecting a chronic stage of white matter injury after TBI based on the presence of significant CC atrophy. *Sarm1* −/− mice were crossed to Thy1-YFP mice that express yellow fluorescent protein (YFP) in a subset of cortical neurons, including those that extend axons across the CC. The distribution of YFP in axons is a very sensitive indicator of damage since YFP readily fills axonal swellings, which facilitates visualization of such swellings (Gu et al., 2017; Marion et al., 2018; Yu et al., 2017). In addition, immunohistochemistry enables detection of specific markers of axons, myelin, and neuroinflammation in the same tissues. The CC was examined in Thy1-YFP/*Sarm1* +/+ and Thy1-YFP/*Sarm1* −/− littermates at 8 weeks after the sham or TBI procedure (Fig. 4). The CC in Thy1-YFP/*Sarm1* +/+ sham mice is clearly identified by YFP labeling of axons and immunolabeling of myelin for MOG (Fig. 4A). The CC appears thinned after TBI in Thy1-YFP/*Sarm1* +/+ mice (Fig. 4B). The CC morphology in Thy1-YFP/*Sarm1* −/− sham mice appears similar to sham Thy1-YFP/*Sarm1* +/+ littermates (Fig. 4C). Thy1-YFP/*Sarm1* −/− mice do not have marked pathology in CC morphology or myelination after TBI (Fig. 4D).

Axon damage is not fully resolved and persists chronically at this 8 week time point after TBI; rare axonal swellings can be detected by YFP labeling in Thy1-YFP/*Sarm1* +/+ (Fig. 4E) and Thy1-YFP/*Sarm1* −/− (Fig. 4F) mice. Neurofilament immunolabeling of *Sarm1* littermates illustrates axons in both sham and TBI conditions in sagittal sections (Fig. 4G–H), which were taken within the same ROI in the CC as used for the electron microscopy studies (Figs. 1–3). Neurofilament immunolabeling of axons shows a significant reduction after TBI in *Sarm1* +/+ mice that is attenuated in *Sarm1* −/− mice (Fig. 4I).

A similar proportion of the CC area is myelinated in the sham and TBI groups, and in each genotype, based on quantification of MOG immunolabeling (Fig. 4J). Additionally, TUNEL staining revealed only rare apoptotic cells within the CC for all conditions (*Sarm1* +/+ sham = 2.25, *Sarm1* +/+ TBI = 2.69, *Sarm1* −/− sham = 1.62, and *Sarm1* −/− TBI = 2.69 for TUNEL+ cells per section in CC). These findings are in agreement with our early and late stage electron microscopic findings of TBI induced demyelinated axons dispersed within overall areas of myelinated white matter, but without evidences of focal demyelinated lesion areas (Figs. 2, 3).

Importantly, significant thinning of the CC is found after TBI in Thy1-YFP/*Sarm1* +/+ mice that is attenuated in Thy1-YFP/*Sarm1* −/− littermates (Fig. 4K). Therefore, *Sarm1* genetic deletion is sufficient to reduce chronic stage white matter atrophy after TBI.

### 3.5. Sarm1 genetic deletion increases CC astrogliosis in chronic TBI

This *Sarm1* role in CC atrophy raises questions about effects on neuroinflammation, which has been implicated as contributing to chronic white matter atrophy after TBI (Johnson et al., 2013a; Kumar and Loane, 2012; Lozano et al., 2015; Mierzwa et al., 2015; Sullivan et al., 2013). The Thy1-YFP/*Sarm1* +/+ and Thy1-YFP/*Sarm1* −/− cohorts used to evaluate CC atrophy (Fig. 4) were further analyzed to determine if *Sarm1* deletion alters astrogliosis and microglial activation after TBI (Fig. 5). Thy1-YFP/*Sarm1* +/+ sham mice show low levels of immunoreactivity for both GFAP in astrocytes and Iba1 in microglia (Fig. 5A). Both markers illustrate mild responses of astrogliosis and microglial activation at this chronic time point (Fig. 5B). The Thy1-YFP/*Sarm1* −/− mice also show low immunolabeling in sham mice that is more apparent after TBI (Fig. 5C–D). The more intense immunolabeling in both astrocytes and microglia corresponds with shorter, thicker processes indicative of reactive phenotypes after TBI (Fig. 5E–G). Quantification supports the illustrated results of increased GFAP that is actually more extensive in Thy1-YFP/*Sarm1* −/− mice than in Thy1-YFP/*Sarm1* +/+ mice after TBI (Fig. 5H). Although the Iba1 immunolabeling detected reactive cells (Fig. 5G), the overall response was not significantly increased after TBI, as compared to sham, in either genotype by this 8-week time point (Fig. 5I).

### 3.6. Sarm1 deletion effect in CC does not require overt cortical pathology

Finally, we explored the effect of *Sarm1* deletion in the overlying cortical areas with neurons that extend axons through regions of CC atrophy after TBI (Fig. 6). The cortical cytoarchitecture in the Thy1-

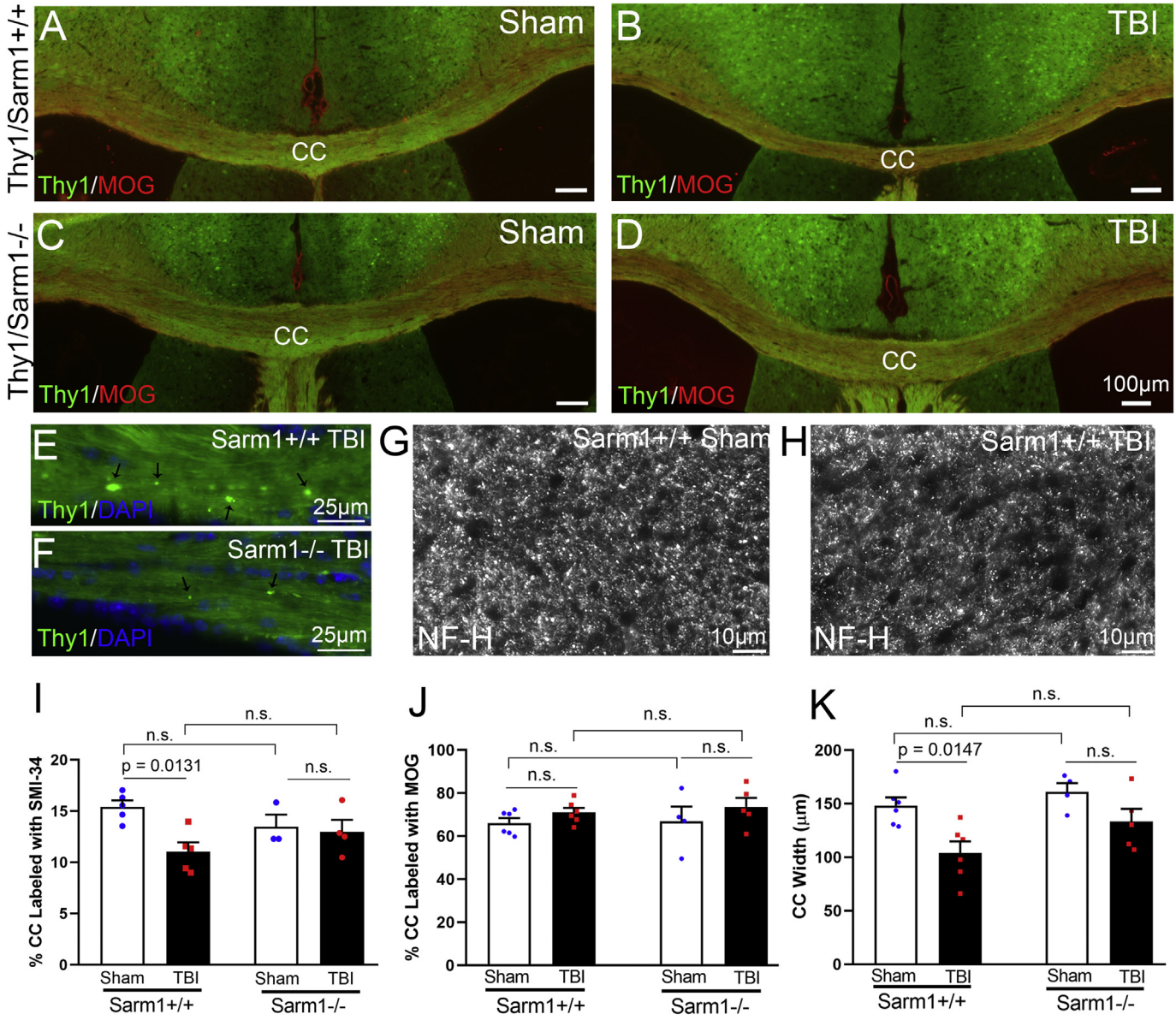


**Fig. 4.** Corpus callosum atrophy at 8 weeks after TBI. A–D, Representative coronal images of Thy1-YFP/*Sarm1*+/+ mice (A, B) and Thy1-YFP/*Sarm1*−/− mice (C, D) at 8 weeks after sham (A, C) or TBI (B, D) procedures. Yellow fluorescent protein (YFP; displayed as green) is present in cortical neurons and the associated axons that extend across the corpus callosum (CC). Myelin is detected by immunohistochemistry for MOG (red). E–F, Higher magnification examples of YFP showing axonal swellings (arrows), a marker of axon damage, at 8 weeks post-TBI in Thy1-YFP/*Sarm1*+/+ mice (E) and in Thy1-YFP/*Sarm1*−/− mice (F). G–H, High magnification examples of CC neurofilament-H (NF-H) labeling of axons with SMI-34 antibody in sagittal sections in *Sarm1*+/+ mice for sham (G) and TBI (H). I, SMI-34 immunolabeling of NF-H in axons is significantly reduced after TBI only in *Sarm1*+/+ mice. J, The proportion of the CC with MOG immunolabeling does not differ between groups. K, TBI significantly reduced the CC width. This CC atrophy was attenuated in *Sarm1*−/− mice. Quantification for MOG and CC width in the coronal plane included *Sarm1*+/+ n = 6 sham, n = 6 TBI; *Sarm1*−/− n = 4 sham, n = 5 TBI. Quantification of NF-H in the sagittal plane included *Sarm1*+/+ n = 5 sham, n = 5 TBI; *Sarm1*−/− n = 3 sham, n = 4 TBI. n.s. = not significant. (For interpretation of the references to colour in this figure legend, the reader is referred to the web version of this article.)

YFP/*Sarm1* cohort was examined in the premotor/motor cortex areas, which are beneath the skull impact site and contain neurons that extend axons through the CC ROI (Gibson et al., 2014; Greig et al., 2013). Thy1-YFP/*Sarm1*+/+ mice do not show marked changes within the cerebral cortex between sham and TBI procedures (Fig. 6A–C). Similarly, Thy1-YFP/*Sarm1*−/− mice also do not show overt differences in cortical cytoarchitecture after either sham or TBI procedures (Fig. 6D–F). More specifically, TBI did not induce cortical atrophy (Fig. 6G), myelin loss (Fig. 6H), astrogliosis (Fig. 6I), or microglial activation (Fig. 6J) in either genotype. Additionally, TUNEL staining revealed only rare apoptotic cells within this cortical region for all conditions (*Sarm1*+/+ sham = 2.29, *Sarm1*+/+ TBI = 1.07, *Sarm1*−/− Sham = 1.37, and *Sarm1*−/− TBI = 1.81 for TUNEL+ cells per section in cortical ROI). This lack of pathological findings in the cortex indicates that protective effects of *Sarm1* deletion likely occur within in the CC, rather than being secondary effects of apoptosis or neuroinflammation associated with the neuronal cell bodies.

## 4. Discussion

This study yields important insights of axon-myelin pathology relative to SARM1 molecular regulation of axon damage, demyelination, and progression of chronic pathology after TBI. The complexity of the TBI pathology reveals a progression of white matter injury that impacts

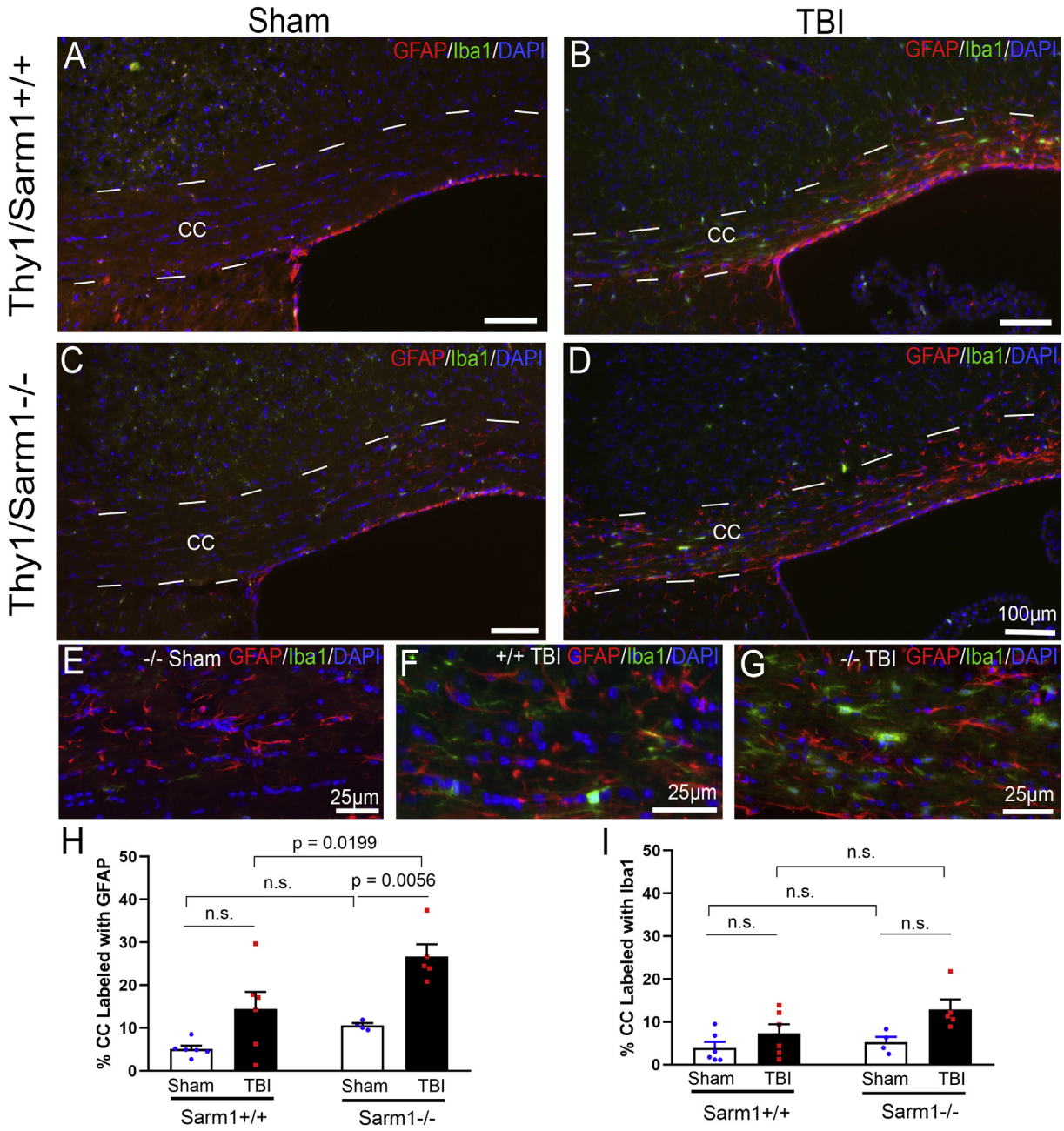


**Fig. 5.** White matter neuroinflammation in chronic TBI. A–D, Representative coronal images of Thy1-YFP/*Sarm1* mice immunostained for the astrocyte marker GFAP (red) and microglial marker Iba1 (green) with DAPI nuclear stain (blue) at 8 weeks after sham (A, C) or TBI (B, D) procedures. Thy1-YFP/*Sarm1*+/+ mice (A, B) have low levels of immunoreactivity for GFAP or Iba1 in the corpus callosum (CC) of sham mice (A), while both markers are increased after TBI (B). In Thy1-YFP/*Sarm1*−/− mice (C, D) immunolabeling for GFAP and Iba1 is also low in sham mice (C) and notably increased after TBI (D). E–G, Higher magnification images to illustrate morphological changes of astrocytes (GFAP) and microglia (Iba1) between the homeostatic morphologies in the sham condition (E) and the reactive phenotypes of shorter, thicker processes with more intense immunolabeling after TBI in Thy1-YFP/*Sarm1*+/+ mice (F) or Thy1-YFP/*Sarm1*−/− mice (G). H–I, In Thy1-YFP/*Sarm1*−/− mice immunolabeling within the CC was significantly increased for GFAP (H) with a lower overall response for Iba1 (I). Note that immunolabeling is displayed in assigned colors that were detected in distinct spectral channels (Iba1 collected in red and GFAP in far-red) that separated from the axonal YFP fluorescence (not shown). *Sarm1*+/+ n = 6 sham, n = 6 TBI; *Sarm1*−/− n = 4 sham, n = 5 TBI. n.s. = not significant. (For interpretation of the references to colour in this figure legend, the reader is referred to the web version of this article.)

the effectiveness of axon protection from *Sarm1* deletion. Furthermore, *Sarm1* deletion modulates myelin parameters, with effects on myelin thickness and demyelination. Importantly, CC atrophy at a chronic stage of progression of white matter injury is attenuated in mice with *Sarm1* deletion.

The high resolution ultrastructural detail afforded by electron microscopy revealed the effect of *Sarm1* deletion relative to multiple features of axon and myelin pathology induced by TBI. Prior neuropathological studies in human and in animal models have recognized distinct features of axon damage after TBI (DiLeonardi et al., 2009; Johnson et al., 2016; Mierzwa et al., 2015). *Sarm1* deletion reduced the extent of early axon damage, which was detected by electron microscopy as either impaired fast axonal transport in swollen axons filled with accumulated vesicles, or as compaction of the axon cytoskeleton (Fig. 1). This result is in agreement with *Sarm1* deletion preventing execution of the conserved axon death molecular pathway for

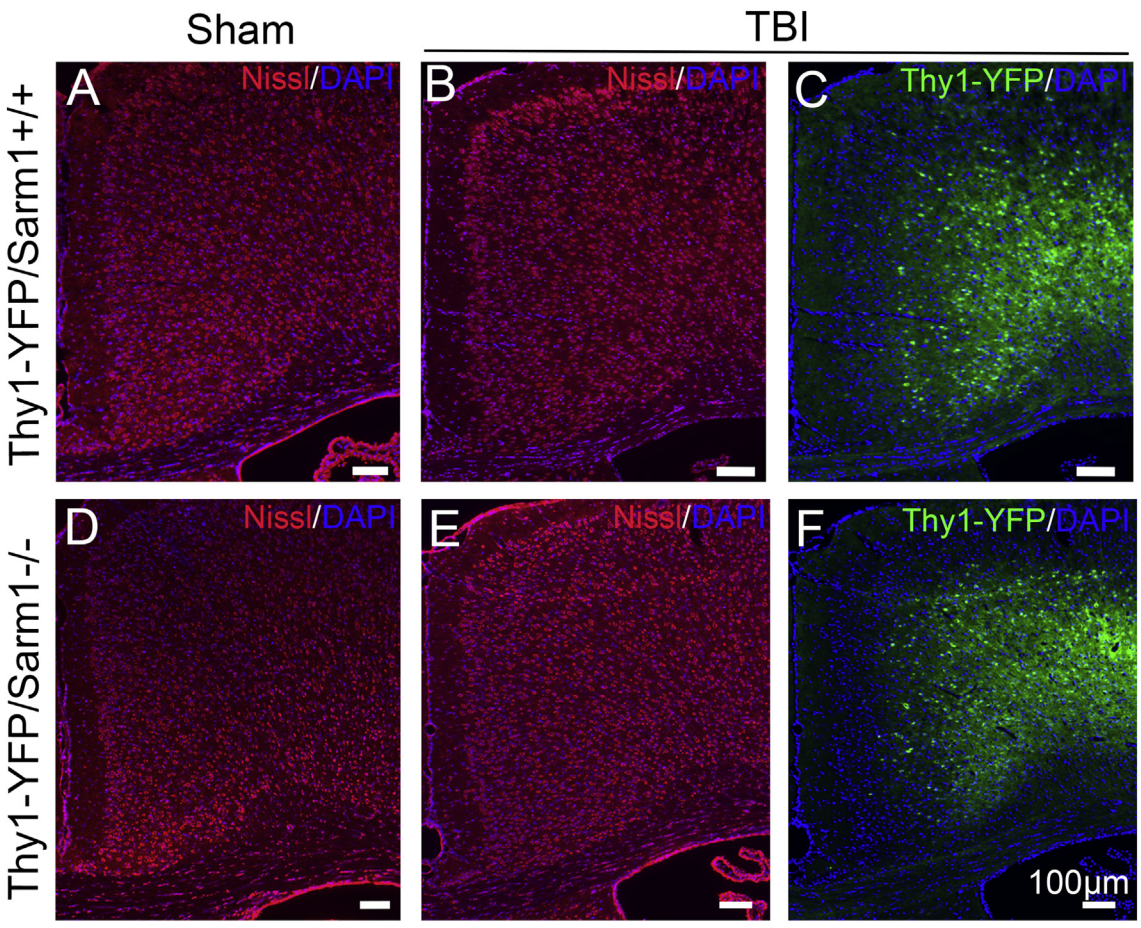


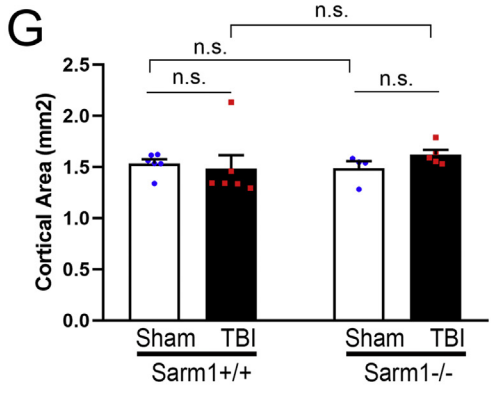


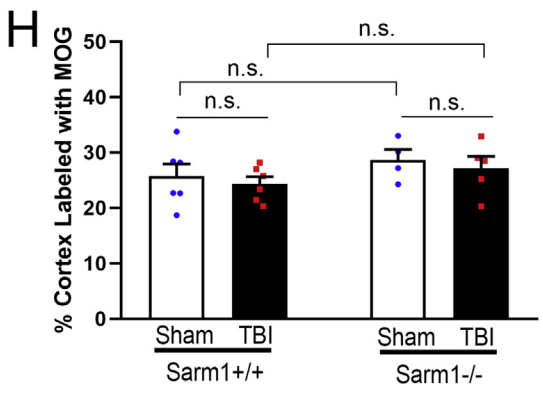


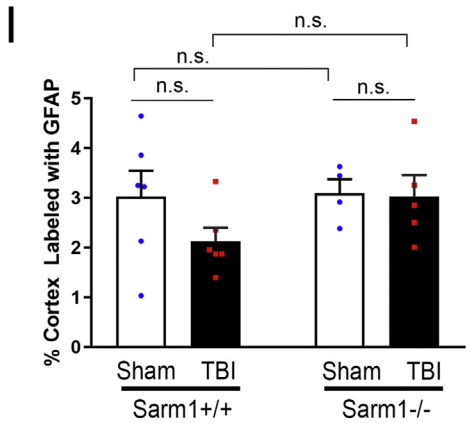


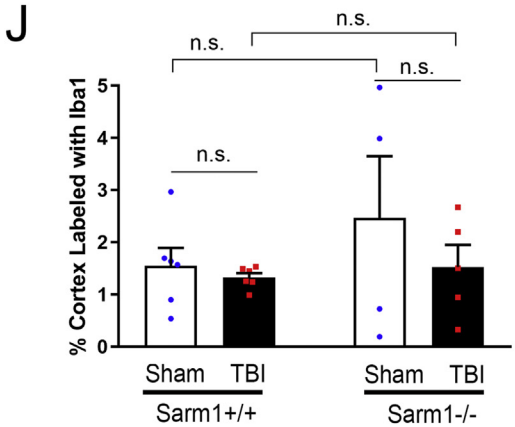


(caption on next page)

**Fig. 6.** Cortical regions under the impact site in chronic TBI. A–F, Representative Nissl and DAPI staining showing cortical neuron cell bodies and nuclei, respectively, in coronal sections from Thy1-YFP/*Sarm*1 mice. Cortical areas under the impact site (on the skull at bregma) include premotor/motor cortex areas that project axons through the corpus callosum, as well as cingulate cortex. Both Thy1-YFP/*Sarm1*+/+ mice (A, B, C) and Thy1-YFP/*Sarm1*−/− mice (D, E, F) have normal appearing cytoarchitecture of the cerebral cortex at 8 weeks after either sham or TBI procedures. Merged Nissl (red) and DAPI (blue) images are shown without YFP to more clearly show the cytoarchitecture. In addition, for the TBI panels, the matching YFP (green) image of the same field is shown merged with DAPI (blue). G–J, TBI did not induce significant cortical atrophy (G), myelin loss (H), astrogliosis (I), or microglial activation (J) in either Thy1-YFP/*Sarm1*+/+ or Thy1-YFP/*Sarm1*−/− mice. *Sarm1*+/+ n = 6 sham, n = 6 TBI; *Sarm1*−/− n = 4 sham, n = 5 TBI. n.s. = not significant. (For interpretation of the references to colour in this figure legend, the reader is referred to the web version of this article.)

Wallerian degeneration. At the later 6 week time post-TBI, the population of damaged axons continued to be observed by electron microscopy but was not reduced with *Sarm1* deletion (Fig. 3). Others have reported significantly reduced axon damage in *Sarm1* knockout mice at 2 and 48 h after TBI using immunolabeling for β-amyloid precursor protein, although at 7, 14 or 28 days the axon damage was not detected as above sham condition using this technique (Henninger et al., 2016). It should also be noted that while our ultrastructural analysis enables very sensitive and specific detection of axon damage, dynamic effects of *Sarm1* deletion on the population of damaged axons may be difficult to distinguish. For example, the axon damage observed at 6 weeks post-injury could reflect multiple processes, including a) lack of continued axon protection for damage initiated during the later stage pathology, b) delayed appearance of damage that was initiated earlier, and/or c) accumulation of damaged axons due to slowed phagocytosis.

These studies also demonstrated that *Sarm1* deletion did not prevent TBI induced mitochondrial swelling in axons (Fig. 1). Mitochondrial swelling has long been recognized as an early feature of axonal injury associated with Wallerian degeneration (Vial, 1958; Webster, 1962). In inflammatory white matter lesions, the earliest ultrastructural evidence of axon damage is mitochondrial abnormalities, which occur along with axon swellings during an initial reversible stage that precedes demyelination and axon fragmentation (Nikic et al., 2011). Mitochondrial dysfunction contributes to SARM1 execution of the axon death pathway, possibly at multiple stages. SARM1 is activated under oxidative stress conditions but SARM1 also inhibits mitochondrial respiration (Murata et al., 2018). In addition, *Sarm1* deletion protects neurons from accumulation of reactive oxygen species (Summers et al., 2014). However, *Sarm1* deletion that blocks calcium elevation and axon death does not prevent early mitochondrial dynamic changes, and changes in mitochondrial size do not necessarily correlate with the extent of axon degeneration (Loreto et al., 2015). Therefore, our results after TBI, together with these findings in simpler systems, indicate that TBI induced mitochondrial changes can be dissociated from *Sarm1* deletion, or may occur upstream of SARM1 activation, in the process of axon degeneration.

Evaluation of *Sarm1* deletion relative to myelin pathology particularly gained from an electron microscopy approach (Fig. 2). Proper axon function is highly dependent on intact ensheathing myelin structure and axon-myelin molecular interactions (Nave, 2010; Ontaneda et al., 2017b). During postnatal development, the most rapid increase in the proportion of myelinated axons and number of myelin lamellae in the mouse CC occurs prior to the time of injury at 8 weeks of age, yet continues to increase more gradually throughout adult life (Sturrock, 1980). Interestingly, *Sarm1* deletion resulted in significantly reduced myelin thickness (Fig. 2K) and g-ratio values (Fig. S2) in sham mice from the 3 day cohort that was not found in the 6 week cohort, which may indicate a hypomyelination phenotype during developmental myelination. Future studies across key time points during developmental myelination would be of interest to characterize the relationship of myelin thickness and axon growth in these *Sarm1*−/− mice, and creation of mice with inducible and conditional regulation of *Sarm1* deletion could be even more informative.

This concussive TBI model results in demyelination of dispersed axons within the white matter in wild type mice (Mierzwa et al., 2015). Demyelination was induced by TBI in *Sarm1*+/+ mice and *Sarm1* deletion attenuated this pathology (Figs. 2G, 3F). *Sarm1* is expressed largely in neurons, but a low transcript level in oligodendrocyte lineage cells could contribute to effects on demyelination (Zhang et al., 2014). The hypomyelination effect observed in sham *Sarm1*−/− mice in the 3 day cohort (see above) is also reflected in the thinner myelin observed after TBI in the 3 day cohort (Fig. 2K). Thinner myelin did not appear to increase vulnerability to demyelination after TBI, since the frequency of demyelinated axons was lower in *Sarm1*−/− mice at both the 3 day and 6 week time points. Our prior studies in this injury have detected relatively low cell death or oligodendrogenesis consistent with a lack of overall myelin loss, but significant myelin remodeling or remyelination was observed in the CC using *NG2Cre ER; mTmG* myelin reporter mice (Sullivan et al., 2013; Mierzwa et al., 2015; Marion et al., 2018). In agreement with this prior characterization, the current analysis detected only rare TUNEL labeled cells per CC and no difference in overall CC myelination (Fig. 4J). Additional approaches would be needed to specifically explore oligodendrocyte and myelin formation changes that could contribute to reduced demyelination of dispersed CC axons in the *Sarm1*−/− mice after TBI. However, attenuation of demyelination may also result from a primary effect of *Sarm1* deletion on axons. Axon diameters are increased by *Sarm1* deletion at 3 days and 6 weeks in sham cohorts but are not different after TBI (Figs. 1M and 3E). The g-ratio is a measure of myelin thickness that takes into account that myelin thickness is proportional to axon diameter in fully myelinated axons, while myelin is thinner during developmental myelination and remyelination (Blakemore, 1981; Duncan et al., 2017). The g-ratio values were only significantly different in the sham 3 day cohort for comparison of *Sarm1*−/− mice versus *Sarm1*+/+ mice (Fig. S2), indicating that *Sarm1* deletion effects on axon diameter did not significantly alter relative myelin thickness after TBI at 3 days or 6 weeks. The demyelination induced by TBI may represent loss of whole segments of myelin sheaths or abnormal nodes of Ranvier and adjacent paranodes, where myelin attaches to the axon (Marion et al., 2018). And, functional deficits consistent with demyelination and conduction block were demonstrated using ex vivo electrical recordings of CC axons (Marion et al., 2018). Therefore, the attenuated demyelination observed with *Sarm1* deletion may be important for maintaining myelin for axon function.

*Sarm1* deletion did not prevent TBI induced formation of myelin outfoldings (Figs. 2–3). This elaboration of myelin sheaths extending away from a degenerating or an intact axon is very rare in the sham condition yet dramatically increased after TBI in the current results and in our prior studies (Mierzwa et al., 2015; Sullivan et al., 2013). These myelin outfoldings appear similar to “redundant” myelin or “excessive” myelin reported in development and in aging (Erwig et al., 2019; Mierzwa et al., 2015; Patzig et al., 2016; Peters and Sethares, 2002; Rosenbluth, 1966; Snaidero et al., 2014; Sturrock, 1976). Myelin outfoldings can occur due to mutations of myelin proteins or scaffolding proteins involved in axon-myelin interactions (Erwig et al., 2019; Patzig et al., 2016). It is not clear why *Sarm1* deletion reduced the length of the myelin outfoldings, but did not prevent formation after TBI. Our ongoing studies are using 3-dimensional reconstructions of serial block-face scanning EM data sets to better evaluate the structure of TBI induced myelin outfoldings (unpublished observation). Myelin outfoldings in some contexts can slow nerve conduction velocity (Erwig et al., 2019; Patzig et al., 2016). In addition, myelin debris can activate

microglia so that myelin outfoldings could fuel processes leading to chronic neuroinflammation (Clarner et al., 2012; Franson and Ronnevi, 1984).

An important finding of the current study is that *Sarm1* deletion reduced the CC atrophy observed at 8 weeks after TBI (Fig. 4). The current data (Figs. 1, 3, 4) and our prior studies show that CC atrophy is not significant at time points up to 6 weeks post-injury, yet is present at 8 weeks (Marion et al., 2018; Mierzwa et al., 2015). This significant CC atrophy indicates progression of white matter pathology between 6 and 8 weeks post-TBI. *Sarm1* deletion both attenuated CC atrophy and also protected against loss of neurofilament immunolabeling of axons at this chronic stage of 8 weeks post-TBI (Fig. 4). Therefore, differences in axon loss appear to contribute to this difference in CC atrophy. Neurofilament immunolabeling is less accurate than electron microscopy for analysis of axon damage (discussed above) but is advantageous as an estimate of axon protection that can be combined with immunolabeling for analysis of cell type-specific markers. Indeed, the increased GFAP immunoreactivity observed in the *Sarm1*−/− mice indicates that astrogliosis could also contribute to the reduced CC atrophy.

Chronic TBI studies have often focused on microglia/macrophage activation as contributing to white matter neurodegeneration and atrophy (Loane et al., 2014; Ramlackhansingh et al., 2011; Shitaka et al., 2011). Our prior TBI studies in this model have characterized the development of astrogliosis and microglial activation as beginning during the first week and continuing at 6 weeks (Mierzwa et al., 2015; Sullivan et al., 2013). However, the current results (Figs. 4, 5) in *Sarm1*−/− mice indicate more specific studies are required to delineate the relationship of astrogliosis and microglial activation relative to the progression of axon damage, demyelination, and white matter atrophy. Relatively low levels of Iba1 and GFAP immunolabeling were observed at 8 weeks post-TBI even though CC atrophy was significant in *Sarm1*+/+ mice (Figs. 4, 5). And unexpectedly, *Sarm1*−/− mice with TBI had increased astrogliosis compared to *Sarm1*+/+ mice (Fig. 5). Since astrocyte and microglial responses can have potential beneficial or detrimental effects, studies using approaches such as deep phenotyping and functional assays will be needed to evaluate this innate immune cell response during the progression of pathology in this white matter injury environment (Filous and Silver, 2016; Goldstein et al., 2016).

Certain limitations of the current study are important to the interpretation of the data. The *Sarm1* knockout employed is not restricted to neurons and so cannot definitively identify reduced axon degeneration as the mechanism underlying the other protective effects on demyelination and atrophy, which could involve indirect effects and non-neuronal cells. However, this model of genetic deletion in all cell types is relevant to understanding the potential effects of a typical pharmacological exposure. Importantly, this genetic deletion is not induced after TBI and so does not allow for a clinically practical time post-injury for the initiation of treatment. The constitutive genetic deletion can also carry forward developmental changes, which needs to be considered for the hypomyelination we observed at the early time point. Indeed, while this genetic deletion model provides specificity, only effects of inactivation continued through to the experiment termination can be evaluated. Our studies indicate that shorter periods of SARM1 inactivation could be important to test in vivo. Further studies with additional approaches, such as gene therapy or small molecule inhibitors relevant to this pathway, may help determine an effective treatment window (Geisler et al., 2019; Ziogas and Koliatsos, 2018). The interaction of SARM1 with related molecular pathways also warrants much more investigation to protect axons without unacceptable effects on restricting neuroplasticity and neuroregeneration (Simon and Watkins, 2018). Additional limitations are inherent in our use of an experimental model that reflects key aspects of human TBI but cannot recapitulate the full human pathology. This model reflects human TBI pathology based on the pattern of traumatic axonal injury of concussive TBI, reduced white matter integrity detected using diffusion tensor imaging, and a chronic stage with significant CC atrophy (Adams et al., 1989; Marion et al., 2018; Mierzwa et al., 2015; Niogi et al., 2008; O'Phelan et al., 2018; Tomaiuolo et al., 2012; Yu et al., 2017). This concussive model can be considered mild in severity since the mice experience loss of consciousness but do not show evidence of overt tissue damage or microhemorrhages on neuroimaging or neuropathology (Mierzwa et al., 2015; Sullivan et al., 2013; Yu et al., 2017). Studies in additional experimental TBI models would be of interest to test the effects of *Sarm1* deletion on additional pathological features given the heterogeneity of human TBI.

## 5. Conclusion

This study shows that *Sarm1* genetic deletion modulates critical components of white matter pathology during the progression of early, late, and chronic time points after experimental TBI. SARM1 is being examined as a promising therapeutic target for diverse forms of axonal injury, including chemotherapy-induced peripheral neuropathy, neurodegenerative disorders, and a subset of traumatic injuries (Simon and Watkins, 2018). The current findings underscore the role of SARM1 in white matter injury after TBI, and provide evidence for TBI as a potential clinical indication for therapeutics targeting this axon death pathway. Importantly, this study also reveals complexities of SARM1 inactivation during the long term progression of white matter pathology after TBI that should be taken into consideration for more accurate evaluation of therapeutic potential.

## Author disclosure statement

The authors declare no competing financial interests.

## Acknowledgements

The authors thank Tuan Le and Xiaomei Zi for their technical assistance. These studies were funded by the U.S. Department of Defense Center for Neuroscience and Regenerative Medicine (CNRM703386; CNRM702720) and Defense Health Agency (ST7434918).

## Appendix A. Supplementary data

Supplementary data to this article can be found online at https://doi.org/10.1016/j.expneurol.2019.113040.

## References

Adams, J.H., Doyle, D., Ford, I., Gennarelli, T.A., Graham, D.I., McLellan, D.R., 1989. Diffuse axonal injury in head injury: definition, diagnosis and grading. Histopathology 15, 49–59.
Armstrong, R.C., Le, T.Q., Flint, N.C., Vana, A.C., Zhou, Y.X., 2006. Endogenous cell repair of chronic demyelination. J. Neuropathol. Exp. Neurol. 65, 245–256.
Armstrong, R.C., Mierzwa, A.J., Marion, C.M., Sullivan, G.M., 2016. White matter involvement after TBI: clues to axon and myelin repair capacity. Exp. Neurol. 275 (Pt 3), 328–333.
Babetto, E., Beirowski, B., Russler, E., Milbrandt, J., DiAntonio, A., 2013. The Phr1 ubiquitin ligase promotes injury-induced axon self-destruction. Cell Rep. 3 (5), 1422–1429.
Blakemore, W.F., 1981. Remyelination in the CNS. Prog. Clin. Biol. Res. 59A, 105–109.
Buki, A., Povlishock, J.T., 2006. All roads lead to disconnection?—traumatic axonal injury revisited. Acta Neurochir. 148, 181–193 (discussion 193-184).
Chung, S., Fieremans, E., Wang, X., Kucukboyaci, N.E., Morton, C.J., Babb, J., Amorapanth, P., Foo, F.A., Novikov, D.S., Flanagan, S.R., Rath, J.F., Lui, Y.W., 2018. White matter tract integrity: An indicator of axonal pathology after mild traumatic brain injury. J. Neurotrauma 35, 1015–1020.
Clarner, T., Diederichs, F., Berger, K., Denecke, B., Gan, L., van der Valk, P., Beyer, C., Amor, S., Kipp, M., 2012. Myelin debris regulates inflammatory responses in an experimental demyelination animal model and multiple sclerosis lesions. Glia 60, 1468–1480.
Coleman, M.P., Freeman, M.R., 2010. Wallerian degeneration, wld(s), and nmnat. Annu. Rev. Neurosci. 33, 245–267.
Conforti, L., Gilley, J., Coleman, M.P., 2014. Wallerian degeneration: an emerging axon

death pathway linking injury and disease. Nat. Rev. Neurosci. 15, 394–409.
Desbois, M., Crawley, O., Evans, P.R., Baker, S.T., Masuho, I., Yasuda, R., Grill, B., 2018. PAM forms an atypical SCF ubiquitin ligase complex that ubiquitinates and degrades NMNAT2. J. Biol. Chem. 293, 13897–13909.
DiLeonardi, A.M., Huh, J.W., Raghupathi, R., 2009. Impaired axonal transport and neurofilament compaction occur in separate populations of injured axons following diffuse brain injury in the immature rat. Brain Res. 1263, 174–182.
Dileonardi, A.M., Huh, J.W., Raghupathi, R., 2012. Differential effects of FK506 on structural and functional axonal deficits after diffuse brain injury in the immature rat. J. Neuropathol. Exp. Neurol. 71, 959–972.
Duncan, I.D., Marik, R.L., Broman, A.T., Heidari, M., 2017. Thin myelin sheaths as the hallmark of remyelination persist over time and preserve axon function. Proc. Natl. Acad. Sci. U. S. A. 114, E9685–E9691.
Erwig, M.S., Patzig, J., Steyer, A.M., Dibaj, P., Heilmann, M., Heilmann, I., Jung, R.B., Kusch, K., Mobius, W., Jahn, O., Nave, K.A., Werner, H.B., 2019. Anillin facilitates septin assembly to prevent pathological outfoldings of central nervous system myelin. Elife 8.
Essuman, K., Summers, D.W., Sasaki, Y., Mao, X., DiAntonio, A., Milbrandt, J., 2017. The SARM1 toll/interleukin-1 receptor domain possesses intrinsic NAD(+) cleavage activity that promotes pathological axonal degeneration. Neuron 93, 1334–1343.
Essuman, K., Summers, D.W., Sasaki, Y., Mao, X., Yim, A.K.Y., DiAntonio, A., Milbrandt, J., 2018. TIR domain proteins are an ancient family of NAD(+)-consuming enzymes. Curr. Biol. 28 (421–430), e424.
Filous, A.R., Silver, J., 2016. Targeting astrocytes in CNS injury and disease: a translational research approach. Prog. Neurobiol. 144, 173–187.
Franson, P., Ronnevi, L.O., 1984. Myelin breakdown and elimination in the posterior funiculus of the adult cat after dorsal rhizotomy: a light and electron microscopic qualitative and quantitative study. J. Comp. Neurol. 223, 138–151.
Gamage, K.K., Cheng, I., Park, R.E., Karim, M.S., Edamura, K., Hughes, C., Spano, A.J., Erisir, A., Deppmann, C.D., 2017. Death receptor 6 promotes Wallerian degeneration in peripheral axons. Curr. Biol. 27, 1250.
Geisler, S., Doan, R.A., Strickland, A., Huang, X., Milbrandt, J., DiAntonio, A., 2016. Prevention of vincristine-induced peripheral neuropathy by genetic deletion of SARM1 in mice. Brain 139, 3092–3108.
Geisler, S., Huang, S.X., Strickland, A., Doan, R.A., Summers, D.W., Mao, X., Park, J., DiAntonio, A., Milbrandt, J., 2019. Gene therapy targeting SARM1 blocks pathological axon degeneration in mice. J. Exp. Med. 216 (2), 294–303.
Gerdts, J., Summers, D.W., Sasaki, Y., DiAntonio, A., Milbrandt, J., 2013. Sarm1-mediated axon degeneration requires both SAM and TIR interactions. J. Neurosci. 33, 13569–13580.
Gerdts, J., Brace, E.J., Sasaki, Y., DiAntonio, A., Milbrandt, J., 2015. SARM1 activation triggers axon degeneration locally via NAD(+) destruction. Science 348, 453–457.
Gerdts, J., Summers, D.W., Milbrandt, J., DiAntonio, A., 2016. Axon self-destruction: new links among SARM1, MAPKs, and NAD+ metabolism. Neuron 89, 449–460.
Gibson, E.M., Purger, D., Mount, C.W., Goldstein, A.K., Lin, G.L., Wood, L.S., Inema, I., Miller, S.E., Bieri, G., Zuchero, J.B., Barres, B.A., Woo, P.J., Vogel, H., Monje, M., 2014. Neuronal activity promotes oligodendrogenesis and adaptive myelination in the mammalian brain. Science 344, 1252304.
Gilley, J., Orsomando, G., Nascimento-Ferreira, I., Coleman, M.P., 2015. Absence of SARM1 rescues development and survival of NMNAT2-deficient axons. Cell Rep. 10, 1974–1981.
Gilley, J., Ribchester, R.R., Coleman, M.P., 2017. Sarm1 deletion, but not Wld(S), confers lifelong rescue in a mouse model of severe axonopathy. Cell Rep. 21, 10–16.
Gilley, J., Mayer, P.R., Yu, G., Coleman, M.P., 2019. Low levels of NMNAT2 compromise axon development and survival. Hum. Mol. Genet. 28, 448–458.
Goldstein, E.Z., Church, J.S., Hesp, Z.C., Popovich, P.G., McTigue, D.M., 2016. A silver lining of neuroinflammation: beneficial effects on myelination. Exp. Neurol. 283, 550–559.
Greig, L.C., Woodworth, M.B., Galazo, M.J., Padmanabhan, H., Macklis, J.D., 2013. Molecular logic of neocortical projection neuron specification, development and diversity. Nat. Rev. Neurosci. 14, 755–769.
Gu, Y., Jukkola, P., Wang, Q., Esparza, T., Zhao, Y., Brody, D., Gu, C., 2017. Polarity of varicosity initiation in central neuron mechanosensation. J. Cell Biol. 216, 2179–2199.
Hartline, D.K., Colman, D.R., 2007. Rapid conduction and the evolution of giant axons and myelinated fibers. Curr. Biol. 17, R29–R35.
Hayes, J.P., Bigler, E.D., Verfaellie, M., 2016. Traumatic brain injury as a disorder of brain connectivity. J. Int. Neuropsychol. Soc.JINS 22, 120–137.
Henninger, N., Bouley, J., Sikoglu, E.M., An, J., Moore, C.M., King, J.A., Bowser, R., Freeman, M.R., Brown Jr., R.H., 2016. Attenuated traumatic axonal injury and improved functional outcome after traumatic brain injury in mice lacking Sarm1. Brain 139, 1094–1105.
James, S., 2019. Global, regional, and national burden of traumatic brain injury and spinal cord injury, 1990–2016: a systematic analysis for the Global Burden of Disease Study 2016. Lancet Neurol. 18, 56–87.
Johnson, V.E., Stewart, J.E., Begbie, F.D., Trojanowski, J.Q., Smith, D.H., Stewart, W., 2013a. Inflammation and white matter degeneration persist for years after a single traumatic brain injury. Brain 136, 28–42.
Johnson, V.E., Stewart, W., Smith, D.H., 2013b. Axonal pathology in traumatic brain injury. Exp. Neurol. 246, 35–43.
Johnson, V.E., Stewart, W., Weber, M.T., Cullen, D.K., Siman, R., Smith, D.H., 2016. SNTF immunostaining reveals previously undetected axonal pathology in traumatic brain injury. Acta Neuropathol. 131, 115–135.
Kim, Y., Zhou, P., Qian, L., Chuang, J.Z., Lee, J., Li, C., Iadecola, C., Nathan, C., Ding, A., 2007. MyD88-5 links mitochondria, microtubules, and JNK3 in neurons and regulates neuronal survival. J. Exp. Med. 204, 2063–2074.
Kumar, A., Loane, D.J., 2012. Neuroinflammation after traumatic brain injury: opportunities for therapeutic intervention. Brain Behav. Immun. 26, 1191–1201.
Lee, Y., Morrison, B.M., Li, Y., Lengacher, S., Farah, M.H., Hoffman, P.N., Liu, Y., Tsingalia, A., Jin, L., Zhang, P.W., Pellerin, L., Magistretti, P.J., Rothstein, J.D., 2012. Oligodendroglia metabolically support axons and contribute to neurodegeneration. Nature 487, 443–448.
Lipton, M.L., Gellella, E., Lo, C., Gold, T., Ardekani, B.A., Shifteh, K., Bello, J.A., Branch, C.A., 2008. Multifocal white matter ultrastructural abnormalities in mild traumatic brain injury with cognitive disability: a voxel-wise analysis of diffusion tensor imaging. J. Neurotrauma 25, 1335–1342.
Loane, D.J., Kumar, A., Stoica, B.A., Cabatbat, R., Faden, A.I., 2014. Progressive neurodegeneration after experimental brain trauma: association with chronic microglial activation. J. Neuropathol. Exp. Neurol. 73, 14–29.
Loreto, A., Di Stefano, M., Gering, M., Conforti, L., 2015. Wallerian degeneration is executed by an NMN-SARM1-dependent late Ca(2+) influx but only modestly influenced by mitochondria. Cell Rep. 13, 2539–2552.
Lozano, D., Gonzales-Portillo, G.S., Acosta, S., de la Pena, I., Tajiri, N., Kaneko, Y., Borlongan, C.V., 2015. Neuroinflammatory responses to traumatic brain injury: etiology, clinical consequences, and therapeutic opportunities. Neuropsychiatr. Dis. Treat. 11, 97–106.
Malapati, H., Millen, S.M., W., J.B., 2017. The axon degeneration gene SARM1 is evolutionarily distinct from other TIR domain-containing proteins. Mol. Genet. Genom. 292, 909–922.
Marion, C.M., Radomski, K.L., Cramer, N.P., Galdzicki, Z., Armstrong, R.C., 2018. Experimental traumatic brain injury identifies distinct early and late phase axonal conduction deficits of white matter pathophysiology, and reveals intervening recovery. J. Neurosci. 38, 8723–8736.
Marmarou, C.R., Walker, S.A., Davis, C.L., Povlishock, J.T., 2005. Quantitative analysis of the relationship between intra- axonal neurofilament compaction and impaired axonal transport following diffuse traumatic brain injury. J. Neurotrauma 22, 1066–1080.
Maxwell, W.L., Bartlett, E., Morgan, H., 2015. Wallerian degeneration in the optic nerve stretch-injury model of traumatic brain injury: a stereological analysis. J. Neurotrauma 32, 780–790.
Mi, S., Lee, X., Hu, Y., Ji, B., Shao, Z., Yang, W., Huang, G., Walus, L., Rhodes, K., Gong, B.J., Miller, R.H., Pepinsky, R.B., 2011. Death receptor 6 negatively regulates oligodendrocyte survival, maturation and myelination. Nat. Med. 17, 816–821.
Mierzwa, A.J., Marion, C.M., Sullivan, G.M., McDaniel, D.P., Armstrong, R.C., 2015. Components of myelin damage and repair in the progression of white matter pathology after mild traumatic brain injury. J. Neuropathol. Exp. Neurol. 74, 218–232.
Morrison, B.M., Lee, Y., Rothstein, J.D., 2013. Oligodendroglia: metabolic supporters of axons. Trends Cell Biol. 23, 644–651.
Murata, H., Khine, C.C., Nishikawa, A., Yamamoto, K.I., Kinoshita, R., Sakaguchi, M., 2018. C-Jun N-terminal kinase (JNK)-mediated phosphorylation of SARM1 regulates NAD(+) cleavage activity to inhibit mitochondrial respiration. J. Biol. Chem. 293, 18933–18943.
Nave, K.A., 2010. Myelination and the trophic support of long axons. Nat. Rev. Neurosci. 11, 275–283.
Neukomm, L.J., Burdett, T.C., Seeds, A.M., Hampel, S., Coutinho-Budd, J.C., Farley, J.E., Wong, J., Karadeniz, Y.B., Osterloh, J.M., Sheehan, A.E., Freeman, M.R., 2017. Axon death pathways converge on Axundead to promote functional and structural axon disassembly. Neuron 95 (78–91), e75.
Nikic, I., Merkler, D., Sorbara, C., Brinkoetter, M., Kreutzfeldt, M., Bareyre, F.M., Bruck, W., Bishop, D., Misgeld, T., Kerschensteiner, M., 2011. A reversible form of axon damage in experimental autoimmune encephalomyelitis and multiple sclerosis. Nat. Med. 17, 495–499.
Niogi, S.N., Mukherjee, P., Ghajar, J., Johnson, C., Kolster, R.A., Sarkar, R., Lee, H., Meeker, M., Zimmerman, R.D., Manley, G.T., McCandliss, B.D., 2008. Extent of microstructural white matter injury in postconcussive syndrome correlates with impaired cognitive reaction time: a 3 T diffusion tensor imaging study of mild traumatic brain injury. Am. J. Neuroradiol. 29, 967–973.
Ontaneda, D., Cohen, J.A., Amato, M.P., 2017a. Clinical outcome measures for progressive MS trials. Multiple Scler. 23, 1627–1635.
Ontaneda, D., Thompson, A.J., Fox, R.J., Cohen, J.A., 2017b. Progressive multiple sclerosis: prospects for disease therapy, repair, and restoration of function. Lancet 389, 1357–1366.
O'Phelan, K.H., Otoshi, C.K., Ernst, T., Chang, L., 2018. Common patterns of regional brain injury detectable by diffusion tensor imaging in otherwise normal-appearing white matter in patients with early moderate to severe traumatic brain injury. J. Neurotrauma 35, 739–749.
Osterloh, J.M., Yang, J., Rooney, T.M., Fox, A.N., Adalbert, R., Powell, E.H., Sheehan, A.E., Avery, M.A., Hackett, R., Logan, M.A., MacDonald, J.M., Ziegenfuss, J.S., Milde, S., Hou, Y.J., Nathan, C., Ding, A., Brown Jr., R.H., Conforti, L., Coleman, M., Tessier-Lavigne, M., Zuchner, S., Freeman, M.R., 2012. dSarm/Sarm1 is required for activation of an injury-induced axon death pathway. Science 337, 481–484.
Pan, S., Chan, J.R., 2017. Regulation and dysregulation of axon infrastructure by myelinating glia. J. Cell Biol. 216, 3903–3916.
Patzig, J., Erwig, M.S., Tenzer, S., Kusch, K., Dibaj, P., Mobius, W., Goebbels, S., Schaeren-Wiemers, N., Nave, K.A., Werner, H.B., 2016. Septin/anillin filaments scaffold central nervous system myelin to accelerate nerve conduction. eLife 5.
Peters, A., Sethares, C., 2002. Aging and the myelinated fibers in prefrontal cortex and corpus callosum of the monkey. J. Comp. Neurol. 442, 277–291.
Pieper, A.A., McKnight, S.L., 2019. Benefits of enhancing nicotinamide adenine dinucleotide levels in damaged or diseased nerve cells. Cold Spring Harb. Symp. Quant. Biol. https://doi.org/10.1101/sqb.2018.83.037622. Feb 20. pii: 037622, ahead of print.

Ramlackhansingh, A.F., Brooks, D.J., Greenwood, R.J., Bose, S.K., Turkheimer, F.E., Kinnunen, K.M., Gentleman, S., Heckemann, R.A., Gunanayagam, K., Gelosa, G., Sharp, D.J., 2011. Inflammation after trauma: microglial activation and traumatic brain injury. Ann. Neurol. 70, 374–383.

Reeves, T.M., Smith, T.L., Williamson, J.C., Phillips, L.L., 2012. Unmyelinated axons show selective rostrocaudal pathology in the corpus callosum after traumatic brain injury. J. Neuropathol. Exp. Neurol. 71, 198–210.

Reynolds, E.S., 1963. The use of lead citrate at high pH as an electron-opaque stain in electron microscopy. J. Cell Biol. 17, 208–212.

Rosenbluth, J., 1966. Redundant myelin sheaths and other ultrastructural features of the toad cerebellum. J. Cell Biol. 28, 73–93.

Rutgers, D.R., Fillard, P., Paradot, G., Tadie, M., Lasjaunias, P., Ducreux, D., 2008. Diffusion tensor imaging characteristics of the corpus callosum in mild, moderate, and severe traumatic brain injury. Am. J. Neuroradiol. 29, 1730–1735.

Shitaka, Y., Tran, H.T., Bennett, R.E., Sanchez, L., Levy, M.A., Dikranian, K., Brody, D.L., 2011. Repetitive closed-skull traumatic brain injury in mice causes persistent multifocal axonal injury and microglial reactivity. J. Neuropathol. Exp. Neurol. 70, 551–567.

Simon, D.J., Watkins, T.A., 2018. Therapeutic opportunities and pitfalls in the treatment of axon degeneration. Curr. Opin. Neurol. 31, 693–701.

Smith, D.H., Hicks, R., Povlishock, J.T., 2013. Therapy development for diffuse axonal injury. J. Neurotrauma 30, 307–323.

Snaidero, N., Mobius, W., Czopka, T., Hekking, L.H., Mathisen, C., Verkleij, D., Goebbels, S., Edgar, J., Merkler, D., Lyons, D.A., Nave, K.A., Simons, M., 2014. Myelin membrane wrapping of CNS axons by PI(3,4,5)P3-dependent polarized growth at the inner tongue. Cell 156, 277–290.

Sturrock, R.R., 1976. Changes in neurologia and myelination in the white matter of aging mice. J. Gerontol. 31, 513–522.

Sturrock, R.R., 1980. Myelination of the mouse corpus callosum. Neuropathol. Appl. Neurobiol. 6, 415–420.

Sullivan, G.M., Mierzwa, A.J., Kijpaisalratana, N., Tang, H., Wang, Y., Song, S.K., Selwyn, R., Armstrong, R.C., 2013. Oligodendrocyte lineage and subventricular zone response to traumatic axonal injury in the corpus callosum. J. Neuropathol. Exp. Neurol. 72, 1106–1125.

Summers, D.W., DiAntonio, A., Milbrandt, J., 2014. Mitochondrial dysfunction induces Sarm1-dependent cell death in sensory neurons. J. Neurosci. 34, 9338–9350.

Summers, D.W., Gibson, D.A., DiAntonio, A., Milbrandt, J., 2016. SARM1-specific motifs in the TIR domain enable NAD+ loss and regulate injury-induced SARM1 activation. Proc. Natl. Acad. Sci. U. S. A. 113, E6271–e6280.

Summers, D.W., Milbrandt, J., DiAntonio, A., 2018. Palmitoylation enables MAPK-dependent proteostasis of axon survival factors. Proc. Natl. Acad. Sci. U. S. A. 115, E8746–E8754.

Tomaiuolo, F., Bivona, U., Lerch, J.P., Di Paola, M., Carlesimo, G.A., Ciurli, P., Matteis, M., Cecchetti, L., Forcina, A., Silvestro, D., Azicnuda, E., Sabatini, U., Di Giacomo, D., Caltagirone, C., Petrides, M., Formisano, R., 2012. Memory and anatomical change in severe non missile traumatic brain injury: approximately 1 vs. approximately 8 years follow-up. Brain Res. Bull. 87, 373–382.

Vial, J.D., 1958. The early changes in the axoplasm during wallerian degeneration. J. Biophys. Biochem. Cytol. 4, 551–555.

Webster, H.D., 1962. Transient, focal accumulation of axonal mitochondria during the early stages of wallerian degeneration. J. Cell Biol. 12, 361–383.

Willmott, C., Ponsford, J., Hocking, C., Schonberger, M., 2009. Factors contributing to attentional impairments after traumatic brain injury. Neuropsychology 23, 424–432.

Xiong, X., Hao, Y., Sun, K., Li, J., Li, X., Mishra, B., Soppina, P., Wu, C., Hume, R.I., Collins, C.A., 2012. The Highwire ubiquitin ligase promotes axonal degeneration by tuning levels of Nmnat protein. PLoS Biol. 10 (12), e1001440.

Yin, T.C., Voorhees, J.R., Genova, R.M., Davis, K.C., Madison, A.M., Britt, J.K., Cintron-Perez, C.J., McDaniel, L., Harper, M.M., Pieper, A.A., 2016. Acute axonal degeneration drives development of cognitive, motor, and visual deficits after blast-mediated traumatic brain injury in mice. eNeuro 3.

Yu, F., Shukla, D.K., Armstrong, R.C., Marion, C.M., Radomski, K.L., Selwyn, R.G., Dardzinski, B.J., 2017. Repetitive model of mild traumatic brain injury produces cortical abnormalities detectable by magnetic resonance diffusion imaging, histopathology, and behavior. J. Neurotrauma 34, 1364–1381.

Zhang, Y., Chen, K., Sloan, S.A., Bennett, M.L., Scholze, A.R., O'Keeffe, S., Phatnani, H.P., Guarnieri, P., Caneda, C., Ruderisch, N., Deng, S., Liddelow, S.A., Zhang, C., Daneman, R., Maniatis, T., Barres, B.A., Wu, J.Q., 2014. An RNA-sequencing transcriptome and splicing database of glia, neurons, and vascular cells of the cerebral cortex. J. Neurosci. 34, 11929–11947.

Zhou, Y.X., Pannu, R., Le, T.Q., Armstrong, R.C., 2012. Fibroblast growth factor 1 (FGFR1) modulation regulates repair capacity of oligodendrocyte progenitor cells following chronic demyelination. Neurobiol. Dis. 45, 196–205.

Ziogas, N.K., Koliatsos, V.E., 2018. Primary traumatic axonopathy in mice subjected to impact acceleration: a reappraisal of pathology and mechanisms with high-resolution anatomical methods. J. Neurosci. 38, 4031–4047.